Not to appear in Nonlearned J., 45.

A DIRECT LINKAGE BETWEEN AGN OUTFLOWS IN THE NARROW-LINE REGIONS AND THE X-RAY EMISSION FROM THE ACCRETION DISKS

J. Wang[1,2], D. W. Xu[1,2] and J. Y. Wei[1,2]

wj@bao.ac.cn

ABSTRACT

The origin of outflow in narrow-line region (NLR) of active galactic nucleus (AGN) is studied in this paper by focusing on the relationship between the [O III]λ5007 line profile and the hard X-ray (in a bandpass of 2-10 keV) emission from the central SMBH in type-I AGNs. A sample of 47 local X-ray selected type-I AGNs at $z < 0.2$ is extracted from the 2XMMi/SDSS DR7 catalog that is originally crossmatched by Pineau et al. The X-ray luminosities in an energy band from 2 to 10keV of these luminous AGNs range from 10^{42} to 10^{44} erg s^{-1}. A joint spectral analysis is performed on their optical and X-ray spectra, in which the [O III] line profile is modeled by a sum of several Gaussian functions to quantify its deviation from a pure Gaussian function. The statistics allows us to identify a moderate correlation with a significance level of 2.78σ: luminous AGNs with stronger [O III] blue asymmetry tend to have steeper hard X-ray spectra. By identifying a role of $L/L_{\rm Edd}$ on the correlation at a $2-3\sigma$ significance level in both direct and indirect ways, we argue that the photon index versus asymmetry correlation provides evidence that the AGN's outflow commonly observed in its NLR is related with the accretion process occurring around the central SMBH, which favors the wind/radiation model for the origin of the outflow in luminous AGNs.

Subject headings: galaxies: nuclei - quasars: emission lines - X-ray: galaxies

[1]Key Laboratory of Space Astronomy and Technology, National Astronomical Observatories, Chinese Academy of Sciences

[2]National Astronomical Observatories, Chinese Academy of Sciences

1. INTRODUCTION

It is now generally believed that the feedback from central active galactic nucleus (AGN) plays an important role in the galaxy evolution issue (see reviews in Fabian 2012; Veilleux et al. 2005 and Heckman & Best 2014). A self-regulated super-massive black hole (SMBH) growth and star formation in the host galaxy is potentially realized by sweeping out circumnuclear gas through the feedback process in both galaxies merger and secular evolution scenarios (e.g., Alexander & Hickox 2012; Kormendy & Ho 2013). Both semianalytic models and numerical simulations indicate that this feedback process is useful not only for reproducing the observed $M_{\rm BH}-\sigma_*$ relation, luminosity functions of quasars and normal galaxies (e.g., Fabian 1999; Di Matteo et al. 2005, 2007; Hopkins et al. 2007, 2008; Menci et al. 2008; Silk & Rees 1998; Haehnelt et al. 1998; Khalatyan et al. 2008; Granato et al. 2004; Somerville et al. 2008; Kauffmann & Haehnelt 2000; Springel et al. 2005; Croton et al. 2006), but also for solving the "over cooling" problem in the Λ cold dark matter (ΛCDM) galaxy formation model in which the cooling predicted in galaxy groups and clusters are stronger than the observed one (e.g., Ciotti & Ostriker 2007; Somerville et al. 2008; Hirschmann et al. 2013). By using the SDSS spectroscopic survey, Wang et al. (2011) and Wang (2015) recently suggest a co-evolution between the feedback and host galaxy based on a revealed fact that an AGN with stronger blue asymmetry of the [O III]λ5007 emission line tends to be associated with a younger stellar population.

So far, various methods of the feedback process have been proposed in past decades by a mixture of observational and theoretical studies. These methods include AGN's wind (e.g., Crenshaw et al. 2003; Pounds et al., 2003; Ganguly et al. 2007; Reeves et al. 2009; Dunn et al., 2010; Tombesi et al., 2012), radiation pressure (e.g., Granato et al. 2004; Alexander et al. 2010) and mechanical energy outflow caused by collimated radio jet (e.g., Best et al. 2006; Rosario et al. 2010; Holt et al. 2008; Nesvadba et al. 2008; Guillard et al. 2012).

On the observational ground, there is accumulating evidence that the feedback from central SMBH can drive outflows on various scales (see reviews in Veilleux et al. 2005 and Fabian 2012). In addition to the blueshifted absorption lines in optical, UV and soft X-ray spectra (e.g., Crenshaw et al. 2003; Hamann & Sabra 2004; Wang & Xu, 2015 and references therein), the outflows can be conveniently traced by the blue asymmetry of the [O III]$\lambda\lambda$4959, 5007 doublet and its bulk blueshift with respect to the local system (Heckman et al. 1981; Veron-Cetty et al. 2001; Zamanov et al. 2002; Xu & Komossa 2009; Marziani et al. 2003; Aoki et al. 2005; Boroson 2005; Bian et al. 2005; Komossa et al. 2008; Zhang et al. 2013; Mullaney et al. 2013).

Using the [O III] line profile as a diagnostic of the outflow occurring in AGN's narrow-line region (NLR) enables the studies of the origin of the outflow (feedback) based on large

optical spectroscopic sample. Different results are, however, obtained by various authors. On the one hand, there is ample evidence that the [O III] line blue asymmetry and bulk velocity blueshift are strongly correlated with Eddington ratio ($L/L_{\rm Edd}$, where $L_{\rm Edd} = 1.26 \times 10^{38}(M_{\rm BH}/M_{\odot})$ erg s^{-1} is the Eddington luminosity) of the central AGNs: higher the $L/L_{\rm Edd}$, stronger the blue asymmetry and larger the bulk velocity blueshift will be (e.g., Zhang et al. 2011; Wang et al. 2011; Wang 2015; Boroson 2005; Bian et al. 2005). In addition, the extreme "blue outliers" usually defined as the objects with [O III] bulk blueshift larger than 250km s^{-1} (e.g., Zamanov et al. 2002; Zhou et al. 2006; Komossa et al. 2008) are found to exclusively occur in the AGNs associated with high $L/L_{\rm Edd}$. On the other hand, the relation between the [O III] line profile and radio emission has been reported in the previous studies. Early studies show that the [O III] line width is found to be correlated with radio luminosity at 1.4 GHz ($L_{\rm 1.4GHz}$) for a sample of flat-spectrum radio galaxies (e.g., Heckman et al. 1984; Whittle 1985). Mullaney et al. (2013) and Zakamska & Greene (2014) recently analyzed the [O III] line profile in a large sample of both type I and type II AGNs detected by the SDSS spectroscopic survey. Their results suggest that the [O III] line width is more strongly related to $L_{\rm 1.4GHz}$ than the other AGNs parameters (e.g., line luminosity and $L/L_{\rm Edd}$).

The origin of feedback in local type I AGNs is studied in this paper by focusing on the relationship between the outflow traced by the [O III] line profile and the X-ray emission from the central AGNs. AGNs are well known to be luminous X-ray emitters up to 100 keV. X-ray emission is a powerful tool for identifying nuclear SMBH accretion activity and for studying the accretion process that fuels AGNs, because the luminous X-ray emission from a rapidly accreting AGN is produced in the region very close to the SMBH (e.g., Haardt & Maraschi 1991; Zdziarski et al. 2000; Kawaguchi et al. 2001; Cao 2009).

The paper is organized as follows. The sample selection and spectral analysis are presented in §2 and §3, respectively. The statistical results are shown in §4, and the implications are discussed in §5. A ΛCDM cosmology with parameters $H_0 = 70$ km s^{-1} Mpc^{-1}, $\Omega_{\rm m} = 0.3$, and $\Omega_{\Lambda} = 0.7$ is adopted throughout the paper.

2. SAMPLE SELECTION: Type-I AGNs from the 2XMMi/SDSS-DR7 Catalog

The sample of X-ray selected type-I AGNs used in the current study is extracted from the 2XMMi/SDSS-DR7 catalog, which was originally crossmatched by Pineau et al. (2011) between the incremental Second XMM-Newton Serendipitous Source Catalog (2XMMi, Watson et al. 2009) and the SDSS-DR7 catalog (Abazajian et al. 2009). In the crossmatch, the optical counterpart of an X-ray source is identified by the probability of spatial coin-

cidence estimated from the traditionally adopted likelihood ratio estimator. There are in total 221,012 unique, serendipitous X-ray sources in the 2XMMi catalog. A ∼90% completeness can be achieved for the catalog at a sensitivity of 1×10^{-14} erg s^{-1} cm^{-2} and 9×10^{-14} erg s^{-1} cm^{-2} in the 0.5-2.0 keV and 2.0-12.0 keV bandpasses, respectively. The localization accuracy of the X-ray sources is typical of $2''$. More than 30,000 X-ray point-like sources with a localization accuracy $\geq 5''$ have a SDSS-DR7 optical counterpart with an identification probability larger than 90%.

A sub-sample of X-ray type-I AGNs is selected from the 2XMMi/SDSS-DR7 catalog by requiring that: (1) the probability of an identification is no less than 95%, (2) the angular distance between an individual XMM-Newton X-ray source and its corresponding optical counterpart is less than $3''$, taking into account the SDSS fiber aperture, (3) the redshift is smaller than 0.2, (4) the g-band brightness is brighter than 19 mag, which is necessary for a proper modeling of the optical continuum, and (5) X-ray flux in the 0.2-12 keV bandpass is larger than 1×10^{-14} erg s^{-1} cm^{-2}, which excludes the extracted X-ray spectra with low photon count rates. By focusing on the objects that are classified as quasars according to the spectral type classification given by the SDSS pipelines (Glazebrook et al. 1998; Bromley et al. 1998), there are a total of 82 type-I AGNs fulfilling the above selection criteria, after removing SDSS J093249.57+472522.8 which shows a spectrum typical of a CV star and is incorrectly classified as a quasar by the SDSS pipelines (Yip et al. 2004). By examining the SDSS spectra one by one by eyes, 19 out of the 82 sources are then excluded from the subsequent optical and X-ray spectral analysis, because of their Seyfert-1.8 like spectra (i.e., partially obscured AGNs) in which the continuum is dominated by the starlight from their host galaxies.

3. DATA REDUCTIONS

3.1. XMM-Newton EPIC Spectra

Our X-ray spectral analysis focus on the XMM-Newton EPIC PN (Struder et al. 2001) data. The data are reduced by the SAS v11.0 software[1] and by the corresponding calibration files. The events with patterns of 0-4 are extracted from the PN data for all the 63 X-ray type-I AGNs selected in Section 2, except for one object. Single pixel events (i.e., pattern=0) are extracted for one bright object (SDSS J103438.59+393828.2=KUG 1031+398) since these events are less sensitive to pile-up than other patterns. In the extraction, the bad and hot

[1]http://xmm.esac.esa.int/

pixels are removed from the original image, and the CCD chip gaps avoided. The source spectrum is extracted from a circular aperture at the detected source position. The aperture has a radius of 25″-40″ depending on the brightness of the object. The background is determined from a circular source-free region that is offset from, but close to, the source. The pile-up in the data is checked by the SAS task epatplot. The tasks rmfgen and arfgen are used to generate the needed response files.

There are in total 47 X-ray selected type-I AGNs for the subsequent X-ray spectral modelings. The other 16 objects are excluded either because of the coincidence of the CCD gap or because of the bad X-ray spectral quality beyond 2-3 keV due to their faintness. We fit the extracted spectra over the 0.3-10 keV band by the XSPEC package (Arnaud 1996). The absorption caused by our own galaxy is included in the spectral fitting for each object by taking the column density value from the Leiden/Argentine/Bonn (LAB) Survey (Kalberla et al. 2005). A basic model expressed as *wabs*zwabs*(N× blackbody+powerlaw)* is adopted in the fitting for all of the objects. The power-law photon spectrum is defined as $N(E) \propto E^{-\Gamma}$, where E is the photon energy and Γ is the photon index. We also attempt to reproduce each of the spectra by the neutral reflection model (*pexrav*; Magdziarz & Zdziarski 1995) instead of the simple powerlaw, although no significant improvement (i.e., the difference of the reduced χ^2 is less than 10%) can be obtained from this complicate model. In addition to the basic model, additional components are required for some objects to reproduce the observed spectra. A Gaussian profile is required in three objects (SDSS J091848.61+211717.0, SDSS J140700.40+282714.6 = Mark 668, and SDSS J143452.45+483942.7 =NGC 5683) to model their broad iron Kα emission lines at 6.4 keV (rest frame). At low energy end, the X-ray spectra of SDSS J091848.61+211717.0, SDSS J111706.39+441333.3 (PG 1114+445) and SDSS J124210.61 +331702.6 (WAS 61) are best fitted by an edge-like absorption (*zedge*) due to the K-edge of ions. The best-fit edge energy $E_{\rm edge}$ in rest frame is 0.67 ± 0.04, 0.72 ± 0.01 keV and 0.73 ± 0.01 keV for SDSS J091848.61+211717.0, SDSS J111706.39+441333.3 and SDSS J124210.61+331702.6, respectively. These modeled edge energies suggest that the edge-like absorptions in the three objects are likely caused by the K-shell absorption of O VII ions at 0.74keV. Our best fit model of PG 1114+445 is highly consistent with that was obtained from the *ROSAT* PSPC observation (Laor et al. 1994). As an illustration, Figure 1 shows the X-ray spectral modelings for four objects[2].

[2]We have checked the resulted photon indices by modeling the X-ray spectra in the 2-10keV bandpass with a simple model of *wabs*zwabs*(powerlaw+Gaussian)*. The sample model returns consistent photon indices within their uncertainties when compare with the values obtained from the fittings based on the 0.3-10 KeV band.

3.2. SDSS Optical Spectroscopy

We analyze the one-dimensional optical spectra of the 47 X-ray selected type-I AGNs by the IRAF[3] package as follows. At the beginning, the correction of Galactic extinction is applied to each spectrum according to the color excess, the parameter $E(B-V)$ taken from the Schlegel, Finkbeiner, and Davies Galactic reddening map (Schlegel et al. 1998). An extinction law of the MilkyWay with $R_{\rm V}=3.1$ (Cardelli et al. 1989) is adopted in the correction. Each of the spectra is then transformed to the rest frame, along with the flux correction due to the relativity effect given the redshift provided by the SDSS pipelines.

3.2.1. Continuum modeling and removal

The continuum of each rest-frame spectrum is modeled by the linear sum of several components, they are 1) a broken powerlaw from central AGN, in which the wavelength of the break point and the two spectral indices are not fixed in the continuum modeling, 2) a template of both high order Balmer emission lines and a Balmer continuum from the broad-line region (BLR), 3) an empirical template of the optical Fe II complex, and 4) the eigenspectra of the host galaxy that are built from the standard single stellar population spectral library through the principal component analysis (PCA) method (e.g., Hao et al. 2005; Wang & Wei 2008; Francis et al. 1992). The used spectral library is developed by Bruzual & Charlot (2003). A Galactic extinction curve with $R_V=3.1$ is involved in the modeling to account for the intrinsic extinction due to the host galaxy. A χ^2 minimization is iteratively performed over the rest-frame wavelength range from 3700Å to 7500Å, except for the regions with strong emission lines. Figure 2 illustrates the modeling and removal of the continuum for two typical objects.

The template of the high order Balmer lines (i.e., $\rm H_7-H_{50}$) is taken from the case B recombination model with electron temperature of $T_e=1.5\times10^4$K and electron density of $n_e=10^{8-10}$ cm^{-3}. The model is calculated by Storey & Hummer (1995). The line width of the high order Balmer lines is fixed to be that of the broad component of Hβ, which is determined by our line profile modeling (see below). The Balmer continuum is approximately modeled by the emission from a partially optically thick cloud by following Dietrich et al.

[3]IRAF is distributed by National Optical Astronomy Observatory, which is operated by the Association of Universities for Research in Astronomy, Inc., under cooperative agreement with the National Science Foundation.

(2002, see also in Grandi 1982; Malkan & Sargent 1982):

$$f_\lambda^{\rm BC} = f_\lambda^{\rm BE} B_\lambda(T_e)(1 - e^{-\tau_\lambda}); \lambda \leq \lambda_{\rm BE} \quad (1)$$

where $f_\lambda^{\rm BE}$ is the continuum flux at the Balmer edge $\lambda_{\rm BE} = 3646$Å, $B_\lambda(T_e)$ is the Planck function at an electron temperature[4] of $T_e = 1.0 \times 10^4$K, and τ_λ is the optical depth at wavelength λ. The optical depth at λ is related with the one at the Balmer edge $\tau_{\rm BE}$ as $\tau_\lambda = \tau_{\rm BE}(\lambda/\lambda_{\rm BE})^3$. $\tau_{\rm BE}$ ranges from 0.1 to 2.0, and a typical value of $\tau_{\rm BE} = 0.5$ is adopted in the current Balmer continuum fitting.

We model the optical Fe II complex by using the empirical templates provided in Veron-Cetty et al. (2004). Both the broad and narrow components of the Fe II templates are included in the modeling. Again, the line widths of the broad and narrow Fe II emission are determined from the line profile modeling of the Hβ emission line (see below). With the modeled Fe II complex, its flux (i.e., FeIIλ4570) is measured from the modeled spectrum in the rest-frame wavelength range from 4434 to 4684Å.

3.2.2. Emission line profile modeling

After the removal of the continuum, the emission-line profiles are modeled on each emission-line isolated spectrum for both Hα and Hβ regions (i.e., in the wavelength ranges $\lambda\lambda$6350-6750 and $\lambda\lambda$4800-5050) by the SPECFIT task (Kriss 1994) in the IRAF package. For each object, each emission line is profiled by a linear combination of a set of several Gaussian functions. The line flux ratios of the [O III] and [N II] doublets are fixed to their theoretical values. The line width of the narrow Hα (Hβ) component is fixed to equal to that of [N II] ([O III] core) line, if the resulted two widths are different significantly. In order to properly isolate their [O III]λ5007 line profile (see Section 3.1 below), the broad He Iλ5016 emission line (Veron et al. 2002) is additionally required in the line profile modelings in three objects (i.e., SDSS J111830.28+402554.0, SDSS J134022.86+274058.5 and SDSS J155909.62+350147.4).

The line modelings are schematically presented in the left and right panels in Figure 3 for the Hα and Hβ regions, respectively. As shown in the figure, a linear combination of two or three broad Gaussian functions is usually required to adequately reproduce the observed broad Balmer line profile in most cases. A residual line profile, which is obtained by subtracting the modeled narrow line component (including the modeled forbidden lines)

[4]Malkan & Sargent (1982) shows that the Balmer continuum of AGNs is best fitted with a temperature of $T_e \sim 1.5 \times 10^4$K in the optically thin case or $T_e \sim 10^3$K in the optically thick case.

from the observed profile, is then used to measure the line width and integrated line flux of either broad Hα or Hβ emission line. Figure 4 schematically shows the [O III]λ5007 line profiles modeled by a sum of n Gaussian functions for four typical cases. As illustrated by the figure, generally speaking, a sum of two or three Gaussian functions are adequate to model all the observed [O III] line profiles well.

4. ANALYSIS AND RESULTS

Table 1 lists the results obtained from the above X-ray and optical spectral modelings for the 47 X-ray selected type-I AGNs. The identification of each object and the corresponding redshift given by the SDSS pipelines are listed in Columns (1) and (2), respectively. The full width at half maximum (FWHM) of the broad Hβ emission is tabulated in Column (3). Columns (4) and (12) lists the modeled broad Hα emission line luminosity ($L_{\rm H\alpha}$) and the spectral-fitting-inferred intrinsic X-ray luminosity in a bandpass of 2-10keV ($L_{\rm 2-10keV}$), respectively. The calculated line luminosities are corrected for the local extinction that is inferred from the narrow-line ratio Hα/Hβ by assuming a Balmer decrement for standard case B recombination and a Galactic extinction curve with $R_V = 3.1$. Figure 5 shows a tight relationship between $L_{\rm H\alpha}$ and $L_{\rm 2-10keV}$, which is not related to AGN's NLR. A distribution of the inferred $L_{\rm 2-10keV}$ is plotted in the inert panel of the figure, which shows a range from 10^{42} to 10^{44} erg s^{-1} for $L_{\rm 2-10keV}$. The parameter of RFe defined as the flux ratio between the Fe IIλ4570 and Hβ broad component is tabulated in Column (5). The fitted spectral photon index $\Gamma_{\rm 2-10keV}$ and the corresponding errors at a confidence level of 90% are listed in Column (6). These errors reported by XSPEC package are obtained from our spectral modelings. The measured $\Gamma_{\rm 2-10keV}$ has an average value of 1.86 and a standard deviation of 0.31, which are highly consistent with the typical value of $\Gamma \sim 1.9$ for radio-quiet AGNs (e.g., Zdziarski et al. 1995; Reeves & Turner 2000; Piconcelli et al. 2005; Dadina 2008; Panessa et al. 2008; Zhou & Zhang 2010; Corral et al. 2011; Mateos et al. 2010).

[O III]λ5007 bulk velocity shift Column (7) tabulates the calculated [O III]λ5007 line bulk relative velocity shift defined as $\Delta\upsilon = c\Delta\lambda/\lambda_{0,[\rm OIII]}$, where $\lambda_{0,[\rm OIII]}$ and $\Delta\lambda$ denote the rest-frame wavelength in vacuum of the [O III]λ5007 emission line and the wavelength shift with respect to the narrow Hβ line, respectively. $\Delta\lambda$ is calculated from the modeled line centers as $\Delta\lambda = (\lambda^{\rm ob}_{[\rm OIII]} - \lambda^{\rm ob}_{\rm H\beta}) - (\lambda_{0,[\rm OIII]} - \lambda_{0,\rm H\beta})$ where $\lambda^{\rm ob}_{[\rm OIII]}$ ($\lambda^{\rm ob}_{\rm H\beta}$) and $\lambda_{0,[\rm OIII]}$ ($\lambda_{0,\rm H\beta}$) are the observed line center and the line wavelength in vacuum of the [O III] (Hβ) line, respectively. The narrow Hβ line shows a very small velocity shift relative to the galaxy rest frame (e.g., Komossa et al. 2008), although this point

is argued against by recent studies[5] (e.g., Hu et al. 2008; Bae & Woo 2014; Wang & Xu 2015). A negative value of $\Delta\upsilon$ corresponds to a blueshift, and a positive value to a redshift.

[O III]λ5007 line asymmetry Various "asymmetry" indices are commonly used in previous studies to quantify the asymmetry of [O III] emission line (e.g., Heckman et al. 1981; Whittle 1985; Veilleux 1991; Wang et al. 2011; Liu et al. 2013; Harrison et al. 2014). Briefly speaking, most of these indices (e.g., AI_{20} and AI) give a quantified asymmetry by comparing the measured line widths/centers (in unit of either wavelength or velocity) at different line flux level. By modeling the [O III]λ5007 emission line profile by a sum of several Gaussian profiles, we parametrize the asymmetry of the [O III] lines by a velocity off $\delta\upsilon$ defined as

$$\delta\upsilon = \frac{\sum_{k=1}^{n} a_k(\upsilon_k - \upsilon_p)}{\sum_{k=1}^{n} a_k} \tag{2}$$

where a_k and υ_k is the modeled flux and velocity of the kth Gaussian function, respectively. υ_p denotes the velocity of the Gaussian profile that reproduces the peak of the observed line profile. A negative value of $\delta\upsilon$ denotes a blue asymmetry, and a positive one a red asymmetry. The fitted parameters $\delta\upsilon$ are listed in Columns (10) in Table 1. Figure 6 compares the value of $\delta\upsilon$ used in this study with the parameter of velocity offset $\delta\upsilon_{\rm H14}$ defined in Harrison et al. (2014). We calculate the values of $\delta\upsilon$ for all the 47 X-ray selected type I AGNs by following the definition in Harrison et al. (2014): $\delta\upsilon_{\rm H14} = (\upsilon_{05} + \upsilon_{95})/2$, where υ_{05} and υ_{95} are the velocities at the 5% and 95% percentiles of the overall emission-line, respectively. Although a small systematical difference, one can see from the figure a well correlation between the two parameters.

Uncertainty estimation Except for $\Gamma_{2-10\rm keV}$, all the quoted errors in Table 1 correspond to a 1σ significance level. A proper error propagation is considered in the derivation of the uncertainties for some parameters. Specifically speaking, the uncertainty of RFe is estimated as

$$\Delta{\rm RFe} = {\rm RFe}\sqrt{\Big(\frac{\Delta f_{\rm FeII}}{f_{\rm FeII}}\Big)^2 + \Big(\frac{\Delta f_{\rm H\beta}}{f_{\rm H\beta}}\Big)^2} \tag{3}$$

where $f_{\rm FeII(H\beta)}$ and $\Delta f_{\rm FeII(H\beta)}$ is the measured flux of the optical Fe II complex (broad Hβ emission) and the corresponding uncertainty, respectively. We estimate the final

[5]These results mean that, strictly speaking, the obtained bulk velocity shift of [O III] assesses the bulk relative velocity of high ionized gas with respect to that of low ionized gas.

uncertainty of $\Delta\upsilon$ as

$$\delta\Delta\upsilon = c\sqrt{\left(\frac{\Delta\lambda_{[\mathrm{OIII}]}}{\lambda^0_{[\mathrm{OIII}]}}\right)^2 + \left(\frac{\Delta\lambda_{\mathrm{H}\beta}}{\lambda^0_{\mathrm{H}\beta}}\right)^2} \tag{4}$$

where $\Delta\lambda_{[\mathrm{OIII}](\mathrm{H}\beta)}$ and $\lambda^0_{[\mathrm{OIII}](\mathrm{H}\beta)}$ is the uncertainty of the measured line center and the rest frame wavelength in vacuum of the [O III] (narrow Hβ) emission line, respectively, and c is the light speed. The uncertainty of $\delta\upsilon$ is determined through the formula

$$\mathrm{std}.\delta\upsilon = \sqrt{\sum_{k=1}^{n}(\Delta^2 a'_k + \Delta^2\upsilon'_k)(k \neq p)} \tag{5}$$

where $\Delta a'_k$ is the uncertainty of the weight ($= a_k/\sum a_k$) of the kth Gaussian function and $\Delta\upsilon'_k = \sqrt{\Delta^2\upsilon_k + \Delta^2\upsilon_p}$ $(k \neq p)$. $\Delta\upsilon_k$ and $\Delta\upsilon_k$ is the uncertainty of the velocity of the kth Gaussian function and that of the Gaussian function that reproduces the line peak.

4.1. $\Gamma_{2-10\mathrm{keV}}$ versus [OIII]λ5007 Line Profile

The aim of this paper is to study the relationship between the properties of AGN's X-ray emission and the strength of the feedback traced by the outflow in AGN's NLR. The main results are presented in Figure 7 by using the [O III]λ5007 emission line profile as a diagnose for the outflow occurring in the NLR. The related statistical results are listed in Table 2.

The measured hard X-ray photon index $\Gamma_{2-10\mathrm{keV}}$ is plotted against the resulted [O III] line profile asymmetry parameter $\delta\upsilon$ in the left panel of Figure 7. One can see there is a moderate anti-correlation between the two variables. The relationship means that stronger the blue asymmetry of the [O III]λ5007 emission line, steeper the X-ray spectrum will be. A Spearman rank-order test returns a correlation coefficient of $r_s = -0.411$. The corresponding probability of null correlation from two-tailed is calculated to be $p_s = 0.0054$, which corresponds to a significant level at 2.78σ.

The right panel of Figure 7 shows a similar relationship between the X-ray photon index $\Gamma_{2-10\mathrm{keV}}$ and bulk velocity shift $\Delta\upsilon$ of the [O III]λ5007 line: larger the bulk blueshift of the [O III] line, steeper the X-ray spectrum will be. The two points marked with horizontal arrows at the left side of the plot are the two objects (SDSS J092247.02+512038.0 and SDSS J140621.89+222346.5) with remarkable [O III] line bulk blueshifts, i.e., $\Delta\upsilon \leq -300$ km s^{-1}. These values allow us to classify the two objects as "blue outliers" in which the [O III] bulk blueshift is defined to be larger than 250km s^{-1} (e.g., Zamanov et al. 2002;

Komossa et al. 2008). The measured $\Gamma_{2-10\rm keV}$ of the two objects are as large as 2.15 ± 0.09 and 2.23 ± 0.10. The Spearman rank-order test yields a correlation coefficient of $r_s = -0.483$ with a probability of null correlation of $p_s = 0.0022$ (i.e., a significance level at 3.06σ). The statistics is slightly degraded to $r_s = -0.426$ with $p_s = 0.0087$ (i.e., a significance level at 2.62σ) when the two objects with extremely large bulk blue velocity shifts are excluded.

4.2. Relation with Eigenvector-I Space

We examine the relation between the identified $\Gamma_{2-10\rm keV}$ versus [OIII] line profile correlations and the well documented AGN's Eigenvector-I (EI) space in this section. The EI space is one of the key properties of AGN phenomena. It was first introduced by Boroson & Green (1992, hereafter BG92) for a sample of 87 bright Palomar-Green quasars. In addition to the original anti-correlation between the intensities of the optical Fe II blends and [O III] emission, the space has been subsequently extended to infrared, UV and soft X-ray bands (e.g., Wang et al. 1996; Sulentic et al. 2000a, 2002, 2004; Xu et al. 2003, 2012; Grupe 2004; Laor et al. 1997; Lawrence et al. 1997; Grupe et al. 1999; Vaughan et al. 2001; Zamanov et al. 2002; Marziani et al. 2003; Marziani & Sulentic 2012; Wang et al. 2006). Up to the date, the best EI space that is widely accepted involves three parameters: RFe, FWHM of the Hβ broad component and photon index in soft X-ray, which means the relation with EI space can be studied equivalently by focusing on the two parameters: RFe and FWHM(Hβ) in the current sample. The measured RFe in this paper is in fact found to be correlated with FWHM(Hβ). With the Spearman rank-order test, the correlation coefficient and corresponding probability of null correlation are calculated to be $r_s = -0.397$ and $\rho_s = 0.0071$ (2.69σ), respectively.

Figure 8 illustrates not only the RFe versus FWHM(Hβ) correlation through the symbol size, but also the dependence of the two identified correlations on both two parameters RFe and FWHM(Hβ). The corresponding correlation coefficient matrix is listed in Table 2. Each correlation coefficient and the corresponding probability of the null correlations shown in bracket are calculated through the Spearman rank-order test. One can learn from the table that there is a significant relationship between $\Gamma_{2-10\rm keV}$ and the EI space, which implies that the EI space can be well reproduced in the current X-ray selected type I AGN sample, although the EI space is found to be marginally (moderately) correlated with the line asymmetry index $\delta\upsilon$ (bulk velocity shift $\Delta\upsilon$). A significant anti-correlation between hard X-ray photon index Γ and FWHM of broad Hβ emission line has been firmly established in previous studies (e.g., Brandt et al. 1997; Leighly 1999; Reeves & Turner 2000; Shemmer et al. 2006, 2008; Zhou & Zhang 2010; Jin et al. 2012).

4.3. Role of SMBH Mass and Eddington Ratio

Both SMBH mass ($M_{\rm BH}$) and $L/L_{\rm Edd}$ are critical parameters describing AGN's phenomena (e.g., Shen & Ho 2014). In fact, BG92 first argued that the EI space is potentially driven by $L/L_{\rm Edd}$, which is then confirmed by various authors (e.g., Boroson 2002; Sulentic et al. 2000; Xu et al. 2003, 2012; Marziani et al. 2003b) since the great progress made in the reverberation mapping technique (e.g., Kaspi et al. 2000, 2005; Peterson & Bentz 2006; and see Marziani & Sulentic 2012 and Peterson 2013 for recent reviews). To investigate the role played by the two basic parameters in AGN's feedback process and to explore the physical origin of the identified two new correlations, we here at first estimate the $M_{\rm BH}$ and $L/L_{\rm Edd}$ for the used hard X-ray selected type-I AGNs from their optical spectra, and then study the statistical properties of the estimated $M_{\rm BH}$ and $L/L_{\rm Edd}$.

4.3.1. Derivation of $M_{\rm BH}$ and $L/L_{\rm Edd}$

The calculated $M_{\rm BH}$ and $L/L_{\rm Edd}$ are shown in Columns (8) and (9) in Table 2 for each of the X-ray selected type-I AGNs, respectively. We estimate $M_{\rm BH}$ from the modeled broad Hα line emission for all the 47 X-ray selected type-I AGNs, except for SDSS J015950.24+002340.8, according to the calibrated relationship provided in Greene & Ho (2007, and references therein)

$$M_{\rm BH} = (3.0^{+0.6}_{-0.5}) \times 10^6 \Big(\frac{L_{\rm H\alpha}}{10^{42}\ {\rm ergs\ s^{-1}}}\Big)^{0.45\pm0.03} \Big[\frac{\rm FWHM(H\alpha)}{10^3\ {\rm km\ s^{-1}}}\Big]^{2.06\pm0.06} M_\odot \qquad (6)$$

where $L_{\rm H\alpha}$ is the intrinsic luminosity of the Hα broad component corrected for local extinction and FWHM(Hα) is the line width of broad Hα emission that is resulted from our line profile modeling (Section 3.2.2). With the estimate $M_{\rm BH}$ (i.e., the Eddington luminosity), the Eddington Ratio $L_{\rm bol}/L_{\rm Edd}$ is inferred from a combination of the $L_{5100\mathring{A}}$-$L_{\rm H\alpha}$ relation[6] (Greene & Ho 2005)

$$L_{5100\mathring{A}} = 2.4 \times 10^{43} \Big(\frac{L_{\rm H\alpha}}{10^{42}\ {\rm ergs\ s^{-1}}}\Big)^{0.86}\ {\rm ergs\ s^{-1}} \qquad (7)$$

and the bolometric correction of $L_{\rm bol} = 9\lambda L_\lambda(5100\mathring{A})$ (Kaspi et al. 2000).

Because of its bad observed Hα line profile, the parameters $M_{\rm BH}$ and $L_{\rm bol}/L_{\rm Edd}$ of SDSS J015950.24+002340.8 are estimated from its broad Hβ emission based on a combination

[6]The luminosity relation has a rms scatter around the best-fit line of 0.2dex.

of the calibrations of (Vestergaard & Peterson 2006; Greene & Ho 2005):

$$M_{\rm BH} = 10^{6.67}\Big(\frac{L_{\rm H\beta}}{10^{42}\ {\rm ergs\ s^{-1}}}\Big)^{0.63}\Big[\frac{\rm FWHM(H\beta)}{10^{3}\ {\rm km\ s^{-1}}}\Big]^{2} M_{\odot} \tag{8}$$

and

$$L_{5100\mathring{A}} = 7.31\times10^{43}\Big(\frac{L_{\rm H\beta}}{10^{42}\ {\rm ergs\ s^{-1}}}\Big)^{0.883}\ {\rm ergs\ s^{-1}} \tag{9}$$

where the luminosity of its broad Hβ emission $L_{\rm H\beta}$ is corrected for the local extinction estimated from a combination of a Balmer decrement for standard case B recombination and a Galactic extinction curve with $R_V = 3.1$. Its bolometric luminosity is again obtained from $L_{5100\mathring{A}}$ through the bolometric correction of $L_{\rm bol} = 9\lambda L_{\lambda}(5100\mathring{A})$ (Kaspi et al. 2000).

4.3.2. Statistics

With the estimated $M_{\rm BH}$ and $L/L_{\rm Edd}$, Figure 9 illustrates the role of the two parameters on the identified $\Gamma_{2-10\rm keV}$ versus [OIII]λ5007 line profile correlations. The related correlation coefficient matrix, which is again based on the Spearman rank-order test, is listed in Table 2. On the one hand, the statistics shows that both $\Gamma_{2-10\rm keV}$ and $\delta\upsilon$ are strongly correlated with the estimated $L/L_{\rm Edd}$. The Spearman rank-order tests indicate that the null probabilities of both correlation are smaller than 0.05, which corresponds to a significance level larger than 2σ. Specifically speaking, the significance levels are estimated to be $> 3.89\sigma$ and 2.89σ for the $L/L_{\rm Edd}$-$\Gamma_{2-10\rm keV}$ and $L/L_{\rm Edd}$-$\delta\upsilon$ correlations, respectively. For the $\Gamma_{2-10\rm keV}$ versus $\delta\upsilon$ correlation, AGNs associated with high $L/L_{\rm Edd}$ tend to occupy the soft X-ray spectrum end with strong [O III] blue asymmetry, and ones with low $L/L_{\rm Edd}$ the hard X-ray spectrum end with weak [O III] blue asymmetry. This tendency implies that $L/L_{\rm Edd}$ is a potential physical driver of the $\Gamma_{2-10\rm keV}$ versus $\delta\upsilon$ correlation. On the other hand, in the current sample, $\Delta\upsilon$ is found to be much better correlated with $M_{\rm BH}$ than $L/L_{\rm Edd}$.

5. DISCUSSION

In this paper, we study the origin of AGN's outflow in its NLR by focusing on the relationship between [O III]λ5007 line profile and hard X-ray emission from the central SMBH. A joint spectral analysis in both optics and hard X-ray allows us to reveal a moderate correlation between hard X-ray spectral photon index and [O III] line asymmetry in a sample of 47 local ($z < 0.2$) hard X-ray selected type-I AGNs at a significance level of 2.78σ. It is noted that the results and implications presented here are only relevant for the AGNs that are most luminous in the local Universe.

5.1. $\Gamma_{2-10\rm keV} - \delta\upsilon$ Correlation: A Connection between Accretion Disk and Outflow in NLR

5.1.1. $\Gamma_{2-10\rm keV}$*: an assessment of SMBH accretion*

We argue that the identified hard X-ray spectral photon index versus [O III]λ5007 line asymmetry correlation (i.e., $\Gamma_{2-10\rm keV} - \delta\upsilon$ correlation) provides moderate evidence that the commonly observed AGN's outflow in its NLR (at a radial distance of order 0.1 to 1kpc from the central SMBH, e.g., Osterbrock & Ferland 2006; Heckamn & Best 2014) is related with the accretion process occurring around the central SMBH (i.e., at a distance scale of $\sim 10^{1-2}R_s$ from the central SMBH, where $R_s = 2GM_{\rm BH}/c^2$ is the Schwarzschild radius).

The parameter $\Gamma_{2-10\rm keV}$ is believed to be closely linked with the accretion process around central SMBH. It is generally believed that the hard X-ray emission of AGN is produced in the region very close to the SMBH. A commonly accepted scenario of the hard X-ray emission is the accretion disk-corona model in which a fraction of soft photons from the cold accretion disk is transformed to hard X-ray band through the inverse Compton scattering of the hot electrons with a temperature of $\sim 10^9$K. These electrons are likely accelerated in the corona above the disk by the reconnection of the magnetic fields (e.g., Haardt & Maraschi 1991, 1993; Svensson & Zdziarski 1994; Kawaguchi et al. 2001; Liu et al. 2002, 2003; Cao 2009). This model can successfully explain the observed $L/L_{\rm Edd} - \Gamma$ dependence (e.g., Grupe 2004; Desroches et al. 2009; Gierlinski & Done 2004; Lu & Yu 1999; Porquet et al. 2004; Wang et al. 2004; Bian 2005, Shemmer et al. 2006, 2008; Risaliti et al. 2009; Jin et al. 2012; Zhou & Zhao 2010) as follows. The scattering can efficiently cool the corona above the accretion disk when the disk flux irradiating the corona increases, which finally results in a soft, steep X-ray spectrum at high $L/L_{\rm Edd}$ state (e.g., Pounds et al. 1995).

5.1.2. $L/L_{\rm Edd}$ *as a physical driver*

We further argue that $L/L_{\rm Edd}$ is a potential physical driver of the $\Gamma_{2-10\rm keV} - \delta\upsilon$ correlation. In the current X-ray type-I AGN sample, the dependence of $\Gamma_{2-10\rm keV}$ on $L/L_{\rm Edd}$ can be indirectly learned from the fact that $\Gamma_{2-10\rm keV}$ is found to be correlated with both RFe and FWHM of Hβ (see Table 2) that are basic parameters defining the EI space that is widely believed to be physically driven by $L/L_{\rm Edd}$. A direct relationship between $\Gamma_{2-10\rm keV}$ and $L/L_{\rm Edd}$ can be further identified in the current sample from Table 4 and the bottom panel in Figure 10.

If the above discussion on the physical driver of $\Gamma_{2-10\rm keV} - \delta\upsilon$ correlation is correct, a

dependence of $\delta\upsilon$ on $L/L_{\rm Edd}$ (or EI space) is expected in the current sample. As shown in Table 2 and the top panel of Figure 10 (9), this dependence at a significance level of 2.89σ can be virtually identified in the current sample. The dependence is not hard to be understood because it is generally believed that high $L/L_{\rm Edd}$ favors to drive accretion disc winds (e.g., Proga & Kallman 2002). The line strength from BLR is determined by the vertical structure of the accretion disk, governed by $L/L_{\rm Edd}$, in a way in which a large $L/L_{\rm Edd}$ results in a large X-ray-heated volume that generates strong Fe II complex emission (e.g., BG92). In fact, a correlation between [O III] line profile asymmetry and $L/L_{\rm Edd}$ has been frequently reported in previous studies (e.g., Wang et al. 2011; Wang 2015; Zhang et al. 2011; Boroson 2005; Bian et al. 2005). A deficit of extended emission-line region in the AGNs with high $L/L_{\rm Edd}$ is revealed by Matsuoka (2012). The deficit could be explained either by the AGN's outflow that blows the gas around central SMBH away or by galaxy minor merger that produces radio-loud AGNs that are usually associated with an inefficient accretion.

5.1.3. Disc wind scenario

So far, two major types of feedback have been proposed for AGNs (Fabian 2012). The one is known as the wind/radiation (quasar) mode (e.g., Crenshaw et al. 2003; Pounds et al. 2003; Ganguly et al. 2007; Reeves et al. 2009; Dunn et al. 2010; King & Pounds 2003; Murray et al. 1995; King 2003, 2005; Alexander et al. 2010; King et al. 2011; Zubovas & King 2012; Proga et al. 2000), and the other is the kinetic (radio) mode (e.g., Morganti et al. 2005, 2007; Rosario et al. 2010; Holt et al. 2011; Mahony et al. 2013). As recently reviewed in Fabian (2012), there is a current consensus that the two types of feedback occur in different AGN types. The wind/radiation mode dominantly operates in luminous quasar phase, while the kinetic mode in the less luminous AGNs with low $L/L_{\rm Edd}$.

The linkage between SMBH accretion disk and outflow in NLR that is diagnosed by the [O III] line blue wing suggests that the observed feedback in NLR is rationally originated from the disc winds[7]. A likely scenario is that the blue wing of the [O III] line is likely produced in the inner NLR region (e.g., Bian et al. 2005; Wang et al. 2005) in which the kinematics of the emitting gas is dominated by an acceleration caused by the wind/radiation pressure. The disc wind model has been successfully applied to explain the observed broad ultraviolet absorption lines in a fraction of $\sim 20\%$ quasars and the ultra-fast outflows identified from the blue-shifted X-ray Fe XXV and Fe XXVI absorptions in a few local AGNs (e.g., Tombesi

[7]An exclusion of the scenario involving the interaction between radio jet and interstellar medium can be found in Section 5.2 for the current sample.

et al. 2012; Higginbottom et al. 2014). In the wind/radiation mode, a wind can be launched from the inner accretion disk where the ultraviolet photons are emitted from (e.g., Murray et al. 1995). The hydrodynamic outflow model calculated by Proga et al. (2008) indicates that the wind launched from the accretion disk can extended into the inner NLR, although the specific launch mechanism is still under debate. Possible mechanisms include radiation/line-driven (e.g. Proga et al. 1998, 2000; Laor & Brandt 2002; Proga & Kallman 2004; Nomura et al. 2013; Higginbottom et al. 2014; Hagino et al. 2015), thermally driven (e.g., Begelman et al. 1983; Krolik & Kriss 2000), magnetically driven (e.g., Blandford & Payne 1982; Ferreira 1997; Fukumura et al. 2014; Stepanovs & Fendt 2014) and hybrid models (e.g., Everett 2005; Proga 2003).

5.2. Radio Emission and [OIII] Line Profile

Some previous studies argued that the outflow in NLR is potentially driven by the interaction between radio jet and interstellar medium (e.g., Heckman et al. 1984; Whittle 1985; Brotherton 1996; Holt et al. 2008, 2011; Nesvadba et al. 2008; Whittle & Wilson 2004; Guillard 2012; Morganti et al. 2007; Mahony et al. 2013). This argument is recently reinforced by the studies in Mullaney et al. (2013) and Zakamska & Greene (2014). Both study claim a relation between [O III] line asymmetry and radio luminosity in both type I and II AGNs observed by SDSS.

The role of radio emission played in the [O III] line profile is test for the 47 X-ray selected type I AGNs used in this study. The 47 X-ray AGNs are cross-matched with the FIRST survey catalog (Becker et al. 2003). This environmental cross-match returns only 20 radio objects with detected radio flux exceeding the FIRST limiting flux density (5σ) of 1mJy. The upper limit of radio flux is also taken from the FIRST survey for the each of the other 27 sources, basing upon the reported detection limit at the corresponding celestial position. The luminosity at 1.4 GHz (rest frame) of each radio source at a given redshift z is calculated from the observed integrated flux density at 1.4 GHz f_ν through $L_{1.4\mathrm{GHz}} = 4\pi d_L^2 f_\nu (1+z)^{-1-\alpha}$, where d_L is the luminosity distance, and $\alpha = -0.8$ (e.g., Ker et al., 2012) is the spectral slope defined as $f_\nu \propto \nu^\alpha$. The calculated $L_{1.4\mathrm{GHz}}$ ranges from 10^{22} to 10^{26} W Hz^{-1}, and is plotted against $\Gamma_{2-10\mathrm{keV}}$, $\delta\upsilon$ and $\Delta\upsilon$ in the left, middle and right panel in Figure 11, respectively. The solid blue points denote the sources with a detected radio flux, and the open red points the ones with a flux upper limit. The corresponding statistics based on Kendall's τ is tabulated in Table 2. The values tabulated in line (6) are based on the 20 sources with a detected radio flux, and the ones in line (7) on all the 47 sources through the survival analysis with non-parametric model (e.g., Isobe et al. 1986). Our statistics

shows that in the current sample there is no evidence that both blue wing and bulk velocity blueshift of the [O III] line are driven by the radio emission, i.e., no direct relationship can be identified between $L_{1.4\mathrm{GHz}}$ and $\delta\upsilon$ ($\Delta\upsilon$) in the current sample.

We argue that this result does not mean an inevitable disagreement on the previous studies. At first, one should be bear in mind that the relationships related with radio luminosity are hard to be firmly tested in the current study because its sample size (47 sources) is significantly less than those (with hundreds to thousands of sources) in Mullaney et al. (2013) and Zakamska & Greene (2014). Secondly, the middle panel in Figure 11 shows that the most significant [O III] blue asymmetry tends to occur in the objects with a radio luminosity at 1.4GHz of $10^{22}-10^{24}$W Hz^{-1}, which is close to that observed in Mullaney et al. (2013). Zakamska & Greene (2014) recently proposed that the radio emission in radio-quite AGNs might be produced by the accelerated particles in the interstellar medium of the host galaxy that is shocked by the accretion disk wind.

5.3. Evolution of Feedback in AGNs

We close the paper by a short discussion on the issue of co-evolution of AGN's feedback and its host galaxy. We argue that the revealed X-ray emission (and L/L_{Edd}) dependent outflow seen in NLR is consistent with the coevolution scenario that was suggested in many previous studies. In fact, both AGN's X-ray emission (and L/L_{Edd}) and [O III] line profile have been claimed to be related with the host galaxy stellar population age. On the one hand, Wang et al. (2013) identified a correlation between AGN's hard X-ray spectral index and host galaxy stellar population age in X-ray selected SDSS type-II AGNs: harder the X-ray spectrum, older the host stellar population will be. The important role of L/L_{Edd} in the coevolution issue has been frequently revealed in previous studies by studying the relationship between L/L_{Edd} and host stellar population (e.g., Heckman & Kauffmann 2006; Goulding et al. 2010; Kewley et al. 2006; Wang et al. 2006; Wang & Wei 2008, 2010; Kauffmann et al. 2007; Wild et al. 2007; Wang 2015). On the other hand, by analyzing the optical spectra of narrow emission-line galaxies taken from SDSS survey, Wang et al. (2011) proposed a trend in which AGNs with stronger blue asymmetries tend to be associated with younger stellar populations. This result is recently confirmed and reinforced in Wang (2015) by focusing on partially obscured AGNs. Combining these results implies that the SMBH growth through gas accretion and host galaxy building is potentially linked by the outflow launched from the accretion disk. It is generally believed that a self-regulated SMBH growth and host star formation can be produced by suppressing the star formation in both galaxies merger and secular evolution scenarios through the feedback from central AGN that sweeps

out circumnuclear gas (e.g., Kormendy & Ho 2012; Alexander & Hickox 2012; Fabian 2012; Zubovas et al. 2013).

The dependence of outflow on both SMBH accretion properties and host stellar population suggests that the feedback process, not as a constant, likely evolves with the SMBH growth, and hence with host star formation in an AGN recycle. That means a strong feedback is required to regulate SMBH mass growth and host star formation in the early gas-rich phase associated with soft X-ray spectrum, high $L/L_{\rm Edd}$ and young stellar population. The regulated SMBH growth and host star formation can be, however, achieved by a weak feedback in the late gas-poor phase when both accretion and starforming activities become to be weak.

6. CONCLUSION

We study the origin of AGN's outflow occurring in its NLR by focusing on the relationship between [O III]λ5007 line profile and hard X-ray emission from the central SMBH in a sample of 47 local X-ray selected type I AGNs ($z < 0.2$). These luminous AGNs are extracted from the 2XMMi/SDSS DR7 catalog, and have X-ray luminosities in 2-10keV in a range from 10^{42} to 10^{45} erg s^{-1}. A joint spectral analysis in both optics and hard X-ray on the sample allows us to identify a moderate correlation with a significance level of 2.78σ, in which luminous AGNs with more significant [O III] blue asymmetry tend to be associated with steeper X-ray spectra. Our statistics show that the correlation is related with $L/L_{\rm Edd}$ at a 2-3σ significance level, which suggests that the AGN's outflow in its NLR is likely driven by the accretion process occurring around the central SMBH.

The authors thank the anonymous referee for his/her careful review and helpful suggestions for improving the manuscript. We thanks Dr. X. L. Zhou for the help in X-ray spectral analysis. This study uses the SDSS archive data that was created and distributed by the Alfred P. Sloan Foundation. This work is based on observations obtained with XMM-Newton, an ESA science mission with instruments and contributions directly funded by ESA Member States and the USA (NASA). The study is supported by the National Basic Research Program of China (grant 2009CB824800) and by National Natural Science Foundation of China under grants 11473036 and 11273027.

REFERENCES

Abazajian, K. N., Adelman-McCarthy, J. K., Agueros, M. A., et al. 2009, ApJS, 182, 543

Alexander, D. M., & Hickox, R. C. 2012, New A Rev., 56 ,93

Alexander, D. M., Swinbank, A. M., Smail, Ian, McDermid, R., & Nesvadba, N. P. H. 2010, MNRAS, 402, 2211

Antonucci, R. R. J. 1993, ARA&A, 31, 473

Aoki, K., Kawaguchi, T., & Ohta, K. 2005, ApJ, 618, 601

Arnaud, K. A. 1996, in ASP Conf. Ser. 101, Astronomical Data Analysis Software and Systems V, ed. G. H. Jacoby & J. Barnes (San Francisco, CA: ASP), 17

Bae, Hyun-Jin, & Woo, Jong-Hak. 2014, ApJ, 795, 30

Begelman, M. C., McKee, C. F., & Shields, G. A. 1983, ApJ, 271, 70

Best, P. N., Kaiser, C. R., Heckman, T. M., & Kauffmann, G. 2006, MNRAS, 368, 67

Bian, W. H., Yuan, Q. R., & Zhao, Y. H. 2005, MNRAS, 364, 187

Blandford, R. D., & Payne, D. G. 1982, MNRAS, 199, 883

Boroson, T. A. 2002, ApJ, 565, 78

Boroson, T. A. 2005, AJ, 130, 381

Boroson, T. A., & Green, R. F. 1992, ApJS, 80, 109

Brandt, W. N., Mathur, S., Reynolds, C. S., & Elvis, M. 1997, MNRAS, 292, 407

Bromley, B. C., Press, W. H., Lin, H., & Kirshner, R. P. 1998, ApJ, 505, 25

Bruzual, G., & Charlot, S. 2003, MNRAS, 344, 100

Cao, X. 2009, MNRAS, 394, 207

Cardelli, J. A., Clayton, G. C., & Mathis, J. S. 1989, ApJ, 345, 245

Ciotti, L., & Ostriker, J. P. 2007, 665, 1038

Croton, D. J., Springel, V., White, S. D. M., et al. 2006, MNRAS, 365, 1

Crenshaw, D. M., et al. 2003, ApJ, 594, 116

Dietrich, M., Hamann, F., Shields, J. C., Constantin, A., Vestergaard, M., Chaffee, F., Foltz, C. B., & Junkkarinen, V. T. 2002, ApJ, 581, 912

Di Matteo, P., Combes, F., Melchior, A.-L., & Semelin, B. 2007, A&A, 468, 61

Di Matteo, T., Springel, V., & Hernquist, L. 2005, Nature, 433, 604

Desroches, L., Greene, J. E., & Ho, L. C. 2009, ApJ, 698, 1515

Du, P., Wang, J. M., Hu, C., Valls-Gabaud, D., Baldwin, J, A., Ge, J. Q., & Xue, S. J. 2014, MNRAS, 438, 2828

Dunn, J. P., et al. 2010, ApJ, 709, 611

Everett, J. E. 2005, ApJ, 631, 689

Fabian, A. C. 1999, MNRAS, 308, L39

Fabian, A. C. 2012, ARA&A, 50, 455

Ferreira, J. 1997, A&A, 319, 340

Francis, P. J., Hewett, P. C., Foltz, C. B., & Chaffee, F. H. 1992, ApJ, 398, 476

Fukumura, K., Tombesi, F., Kazanas, D., Shrader, C., Behar, E., & Contopoulos, I. 2014, ApJ, 780, 120

Ganguly, R., Brotherton, M. S., Cales, S., Scoggins, B., Shang, Z., & Vestergaard, M. 2007, ApJ, 665, 990

Gierlinski, M., & Done, C. 2004, MNRAS, 349, L7

Glazebrook, K., Offer, A. R., & Deeley, K. 1998, ApJ, 492, 98

Goulding, A. D., Alexander, D. M., Lehmer, B. D., & Mullaney, J. R. 2010, MNRAS, 406, 597

Granato, G. L., De Zotti, G., Silva, L., Bressan, A., & Danese, L. 2004, ApJ, 600, 580

Grandi, S. A. 1982, ApJ, 255, 25

Greene, J. E., & Ho, L. C. 2005, ApJ, 630 ,122

Greene, J. E., & Ho, L. C. 2007, ApJ, 670 ,92

Grupe, D. 2004, AJ, 127, 1799

Guillard, P., et al. 2012, ApJ, 747, 95

Haehnelt, M. G., Natarajan, P., Rees, M. J. 1998, MNRAS, 300, 817

Hao, L., et al. 2005, AJ, 129, 1795

Haardt, F., & Maraschi, L. 1991, ApJ, 380, 51

Haardt, F., & Maraschi, L. 1993, ApJ, 413, 618

Hagino, K., Odaka, H., Done, C., Gandhi, P., Watanabe, S., Sako, M., & Takahashi, T. 2015, MNRAS, 446, 663

Hamann, F., & Sabra, B. 2004, AGN Physics with the Sloan Digital Sky Survey, Proceedings of a conference held in Princeton, NJ, USA, 27-31 July 2003, Edited by Gordon T. Richards and Patrick B. Hall, ASP Conference Series, Volume 311. San Francisco: Astronomical Society of the Pacific, 203

Harrison, C. M., Alexander, D. M., Mullaney, J. R., & Swinbank, A. M. 2014, MNRAS, 441, 3306

Heckman, T. M., & Best, P. N. 2014, ARA&A, 52, 589

Heckman, T. M., & Kauffmann, G. 2006, New A Rev., 50, 677

Heckman, T. M., Miley, G. K., & Green, R. F. 1984, ApJ, 281, 525

Heckman, T. M., Miley, G. K., van Breugel, W. J. M., & Butcher, H. R. 1981, ApJ, 247, 403

Higginbottom, N., Proga, D., Knigge, C., Long, K. S., Matthews, J. H., & Sim, S. A. 2014, ApJ, 789, 19

Hirschmann, M., Dolag, K., Saro, A., Borgani, S., & Burkert, A. 2014, MNRAS, 442, 2304

Ho, L. C. 2002, ApJ, 564, 120

Holt, J., Tadhunter, C. N., & Morganti, R. 2008, MNRAS, 387, 639

Holt, J., Tadhunter, C. N., Morganti, R., & Emonts, B. H. C. 2011, MNRAS, 410, 1527

Hopkins, P. F., Bundy, K., Hernquist, L., & Ellis, R. S. 2007, ApJ, 659, 976

Hopkins, P. F., Cox, T. J., Keres, D., & Hernquist, L. 2008, ApJS, 175, 390

Hu, C., Wang, J. M., Ho, L. C., et al. 2008, ApJ, 687, 78

Isobe, T., Feigelson, E. D., & Nelson, P. I. 1986, ApJ, 306, 490

Jin, C., Ward, M., & Done, C. 2012, MNRAS, 425, 907

Kalberla, P. M. W., Burton, W. B., Hartmann, D., et al. 2005, A&A, 440, 775

Khalatyan, A., Cattaneo, A., Schramm, M., Gottlber, S., Steinmetz, M., & Wisotzki, L. 2008, MNRAS, 387, 13

Kaspi, S., Maoz, D., Netzer, H., Peterson, B. M., Vestergaard, M., & Jannuzi, B. T. 2005, ApJ, 629, 61

Kaspi, S., Smith, P.S., Netzer, H., Maoz, D., Jannuzi, B.T., & Giveon, U. 2000, ApJ533, 631

Kauffmann, G., & Haehnelt, M. 2000, MNRAS, 311, 576

Kauffmann, G., et al. 2007, ApJS, 173, 357

Kawaguchi, T., Shimura, T., & Mineshige, S. 2001, ApJ, 546, 966

Kewley, L. J., Groves, B., Kauffmann, G., & Heckman, T. 2006, MNRAS, 372, 961

King, A. 2005, ApJ, 596, 27

King, A. 2005, ApJ, 635, 121

King, A. R., & Pounds, K. A. 2003, MNRAS, 345, 657

King, A. R., Zubovas, K., & Power, C. 2011, MNRAS, 415, L6

Komossa, S., Xu, D., Zhou, H., Storchi-Bergmann, T., & Binette, L. 2008, ApJ, 680, 926

Kormendy, J. & Ho, L. C. 2013, ARA&A, 51, 511

Kriss, G. 1994, Adass, 3, 43

Laor, A., & Brandt, W. N. 2002, ApJ, 569, 461

Laor, A., Fiore, F., Elvis, M., Wilkes, B. J., & McDowell, J. C. 1997, ApJ, 477, 93

Laor, A., Fiore, F., Elvis, M., Wilkes, B. J., & McDowell, J. C. 1994, ApJ, 435, 611

Lawrence, A., Elvis, M., Wilkes, B. J., McHardy, I., & Brandt, N. 1997, MNRAS, 285, 897

Leighly, K. M. 1999, ApJS, 125, 317

Liu B. F., Mineshige S., & Shibata K. 2002, ApJ, 572, 173

Liu B. F., Mineshige S., & Ohsuga K., 2003, ApJ, 587, 571

Liu, G. L., Zakamska, N. L.; Greene, J. E., Nesvadba, N. P. H., & Liu, X. 2013, MNRAS, 436, 2576

Lu, Y. J., & Yu, Q. J. 1999, ApJ, 526, 5

Magdziarz, P., & Zdziarski, A. A. 1995, MNRAS, 273, 837

Mahony, E. K., Morganti, R., Emonts, B. H. C., Oosterloo, T. A., & Tadhunter, C. 2013, MNRAS, 435, L58

Malkan, M. A., & Sargent, W. L. W. 1982, ApJ, 254, 22

Marziani, P., & Sulentic, J. W. 2012, New A Rev., 56, 49

Marziani, P., Sulentic, J. W., Zamanov, R., et al. 2003, ApJS, 145, 199

Matsuoka, Y. 2012, ApJ, 2012, 750, 54

Menci, N., Fiore, F., Puccetti, S., & Cavaliere, A. 2008, ApJ, 686, 219

Morganti, R., Holt, J., Saripalli, L., Oosterloo, T. A., & Tadhunter, C. N. 2007, A&A, 476, 735

Morganti, R., Oosterloo, T. A., Tadhunter, C. N., van Moorsel, G., & Emonts, B. 2005, A&A, 439, 521

Mullaney, J. R., Alexander, D. M., Fine, S., Goulding, A. D., Harrison, C. M., & Hickox, R. C. 2013, MNRAS, 433, 622

Nelson, C., Plasek, A., Thompson, A., Gelderman, R., & Monroe, T. 2004, in ASP Conf. Ser. 311, AGN Physics with the Sloan Digital Sky Survey, ed. G. T. Richards & P. B. Hall (San Francisco, CA: ASP), 83

Nesvadba, N. P. H., Lehnert, M. D., De Breuck, C., Gilbert, A. M., & van Breugel, W. 2008, A&A, 491, 407

Nomura, M., Ohsuga, K., Wada, K., Susa, H,, & Misawa, T. 2013, PASJ, 65, 40

Osterbrock D. E., & Ferland G. J. 2006, Astrophysics of Gaseous Nebulae and Active Galactic Nuclei. Univ. Science Books, Mill Valley, CA

Peterson, B. M. 2014, SSRv, 183, 253

Peterson, B. M., & Bentz, M. C. 2006, New A Rev., 50, 769

Pineau, F.-X., Motch, C., Carrera, F., Della Ceca, R., Derriere, S., Michel, L., Schwope, A., & Watson, M. G. 2011, A&A, 527, 126

Porquet, D., Reeves, J. N., OBrien, P., & Brinkmann, W. 2004, A&A, 422, 85

Pounds, K. A., Done, C., & Osborne, J. P. 1995, MNRAS, 277, L5

Pounds, K. A., King, A. R., Page, K. L., & O'Brien, P. T. 2003, MNRAS, 346, 1025

Proga, D. 2003, ApJ, 585, 406

Proga, D., & Kallman, T. R. 2004, ApJ, 616, 688

Proga, D., Ostriker, J. P., & Kurosawa, R. 2008, ApJ, 676, 101

Proga, D., Stone, J. M., & Drew, J. E. 1998, MNRAS, 295, 595

Proga, D., Stone, J. M., & Kallman, T. R. 2000,ApJ, 543, 686

Reeves, J. N., Sambruna, R. M., Braito, V., & Eracleous, M. 2009, ApJ, 702 ,187

Reeves, J. N., & Turner, M. J. L. 2000, MNRAS, 316, 243

Risaliti, G., Young, M., & Elvis, M. 2009, ApJ, 700, 6

Rosario, D. J., Shields, G. A., Taylor, G. B., Salviander, S., & Smith, K. L. 2010, ApJ, 716, 131

Schlegel, D., Finkbeiner, D. P., & Davies, M. 1998, ApJ, 500, 525

Shemmer, O., Brandt, W. N., Netzer, H., Maiolino, R., & Kaspi, S. 2006, ApJ, 646, 29

Shemmer, O., Brandt, W. N., Netzer, H., et al. 2008, ApJ, 682, 81

Shen, Y., & Ho, Luis C. 2014, Nature, 513, 210

Silk, J., & Rees, M. J. 1998, A&A, 331, L1

Somerville, R. S., Hopkins, P. F., Cox, T. J., Robertson, B. E., & Hernquist, L. 2008, MNRAS, 391, 481

Springel, V., White, S. D. M., Jenkins, A., et al. 2005, Nature, 435, 629

Struder, L., Briel, U., Dennerl, K., et al. 2001, A&A, 365, L18

Stepanovs, D., & Fendt, C. 2014, ApJ, 793, 31

Storey, P. J., & Hummer, D. G. 1995, MNRAS, 272, 41

Sulentic, J. W., Marziani, P., & Dultzin-Hacyan, D. 2000, ARA&A, 38, 521

Svensson, R., & Zdziarski, A. A. 1994, ApJ, 436, 599

Tombesi, F., Cappi, M., Reeves, J. N., & Braito, V. 2012, MNRAS, 422, L1

Vaughan, S., Edelson, R., Warwick, R. S., Malkan, M. A., & Goad, M. R. 2001, MNRAS, 327, 673

Vaughan, S., Reeves, J., Warwick, R., & Edelson, R. 1999, MNRAS, 390, 113

Veilleux, S. 1991, ApJS, 75, 357

Veilleux, S., & Osterbrock, D. E. 1987, ApJS, 63, 295

Veron, P., Goncalves, A. C., & Veron-Cetty, M. -P. 2002, A&A, 384, 826

Veron-Cetty, M.-P., Joly, M., & Veron, P. 2004, A&A, 417, 515

Veron-Cetty, M.-P., Veron, P., & Gon alves, A. C. 2001, A&A, 372, 730

Vestergaard, M., & Peterson, B. M. 2006, ApJ, 641, 689

Wang, J. 2015, New A, 37, 15

Wang, J., Mao, Y. F., & Wei, J. Y. 2011, ApJ, 741, 50

Wang, J., & Wei, J. Y. 2008, ApJ, 679, 86

Wang, J., & Wei, J. Y. 2010, ApJ, 719, 1157

Wang, J., Wei, J. Y., & He, X. T. 2006, ApJ, 638, 106

Wang, J., & Xu, D. W. 2015, A&A, 573, 15

Wang, J., Zhou, X. L., & Wei, J. Y. 2013, ApJ, 768, 176

Wang, J. M., Watarai, K. Y., & Mineshige, S. 2004, ApJ, 607, 107

Wang, T., Brinkmann, W., & Bergeron, J. 1996, A&A, 309, 81

Watson, M. G., Schrder, A. C., Fyfe, D., et al. 2009, A&A, 493, 339

Whittle, M. 1985, MNRAS, 213, 33

Whittle, M., & Wilson, A.S. 2004. AJ, 127, 606.

Wild, V., Kauffmann, G., Heckman, T., et al. 2007, MNRAS, 381, 543

Winter, L. M., Lewis, K. T., Koss, M., Veilleux, S., Keeney, B., & Mushotzky, R. F. 2010, ApJ, 710, 503

Xu, D. W., & Komossa, S. 2009, ApJ, 705, 20

Xu, D. W., Komossa, S., Zhou, H, Y., Lu, H. L., Li, C. Grupe, D., Wang, J., & Yuan, W. M. 2012, AJ, 143, 83

Xu, D. W., Komossa, S., Wei, J. Y., Qian, Y., & Zheng, X. Z. 2003, ApJ, 590, 73

Yip, C. W., et al. AJ, 2004, 128, 585

Zakamska, N. L., & Greene, J. E. 2014, MNRAS, 442, 784

Zamanov, R., Marziani, P., Sulentic, J. W., et al. 2002, ApJ, 576, 9

Zdziarski, A. A., Poutanen, J., & Johnson, W. N. 2000, ApJ, 542, 703

Zhang, K., Dong, X., Wang, T., & Gaskell, C. M. 2011, ApJ, 737, 71

Zhang, K., Wang, T., Dong, X., & Lu, H. 2008, ApJ, 685, 109

Zhang, K., Wang, T., Gaskell, C. M., & Dong, X. 2013, ApJ, 762, 51

Zhou, H. Y., Wang, T. G., Yuan, W. M., Lu, H. L., Dong, X. B., Wang, J. X., & Lu, Y. J. 2006, ApJS, 166, 128

Zhou, X. L., & Zhang, S. N. 2010, ApJ, 713, L11

Zubovas, K., & King, A. R. 2012, MNRAS, 426, 2751

Zubovas, K., Nayakshin, S., King, A., & Wilkinson, M. 2013, MNRAS, 433, 3079

Zycki, P. T., Krolik, J. H., Zdziarski, A. A., & Kallman, T. R. 1994, ApJ, 437, 597

Table 1. Properties of the XMM-Newton/SDSS-DR7 type-I AGNs

SDSS	z	FWHM$_{H\beta}$ km s^{-1}	log $\frac{L_{H\alpha}}{\text{erg s}^{-1}}$	RFe	$\Gamma_{2-10keV}$	Δv[b] km s^{-1}	log $\frac{M_{BH}}{M_\odot}$	L/L_{Edd}	δv km s^{-1}	log $\frac{L_X}{\text{erg s}^{-1}}$
(1)	(2)	(3)	(4)	(5)	(6)	(7)	(8)	(9)	(10)	(11)
J010712.04+140844.9	0.0769	1420 ± 220	41.3	0.55 ± 0.09	$2.15^{+0.10}_{-0.10}$	-25.1 ± 39.7	6.19	0.33	-39.1 ± 13.6	42.5
J015950.24+002340.8	0.1627	3240 ± 150	42.7[a]	0.57 ± 0.03	$1.96^{+0.17}_{-0.19}$	56.3 ± 25.0	8.09	0.19	-332.1 ± 185.5	43.7
J030639.58+000343.2	0.1074	1970 ± 50	43.7	0.003 ± 0.002	$1.80^{+0.04}_{-0.04}$	108.3 ± 34.9	8.13	0.38	-85.0 ± 40.9	43.4
J091848.61+211717.0	0.1493	1740 ± 190	43.8	0.05 ± 0.01	$2.04^{+0.19}_{-0.19}$	103.7 ± 45.9	7.80	1.03	-212.8 ± 37.3	42.9
J092247.02+512038.0	0.1598	2610 ± 150	42.3	2.46 ± 0.23	$2.23^{+0.10}_{-0.10}$	-361.2 ± 45.1	6.92	0.44	-349.1 ± 169.6	43.4
J092343.00+225432.6	0.0332	2750 ± 100	41.5	0.25 ± 0.02	$1.90^{+0.02}_{-0.02}$	-42.6 ± 17.6	6.86	0.09	-42.4 ± 29.6	43.6
J093922.89+370943.9	0.1859	1900 ± 150	42.6	0.61 ± 0.05	$2.10^{+0.35}_{-0.39}$	-29.0 ± 42.7	7.13	0.50	-424.7 ± 362.5	43.2
J094439.88+034940.1	0.1554	4410 ± 30	43.0	0.49 ± 0.06	$1.90^{+0.19}_{-0.18}$	-31.4 ± 68.6	8.24	0.08	-165.3 ± 108.6	43.2
J100035.47+052428.5*	0.0786	4020 ± 130	41.8	0.06 ± 0.05	$1.41^{+0.22}_{-0.22}$	22.7 ± 8.9	6.78	0.20	-7.0 ± 3.9	43.2
J102822.84+235125.7*	0.1734	5340 ± 200	42.5	0.01 ± 0.01	$1.89^{+0.19}_{-0.20}$	98.2 ± 18.8	8.05	0.04	$+5.5 \pm 23.8$	43.4
J103059.09+310255.7*	0.1781	5560 ± 330	43.5	0.00 ± 0.00	$1.59^{+0.07}_{-0.07}$	-0.6 ± 27.5	8.71	0.07	$+22.2 \pm 12.9$	44.3
J103349.93+631830.4	0.1555	1950 ± 410	42.8	0.03 ± 0.01	$2.11^{+0.14}_{-0.13}$	.....	7.48	0.28	-42.9 ± 40.8	43.1
J103438.59+393828.2	0.0431	870 ± 90	42.1	0.16 ± 0.02	$2.56^{+0.17}_{-0.17}$	-27.3 ± 15.7	6.61	0.53	-191.0 ± 32.9	42.3
J105143.89+335926.7	0.1671	3880 ± 160	43.3	0.18 ± 0.01	$1.92^{+0.04}_{-0.04}$	75.2 ± 41.0	8.15	0.17	-1.1 ± 5.7	44.0
J110101.77+110248.9*	0.0356	7210 ± 250	41.9	0.01 ± 0.01	$1.66^{+0.05}_{-0.03}$	0.1 ± 16.1	7.79	0.02	$+5.5 \pm 8.0$	43.0
J111706.39+441333.3	0.1438	5180 ± 170	44.2	0.02 ± 0.01	$1.52^{+0.02}_{-0.02}$	-12.6 ± 49.0	8.88	0.21	-124.7 ± 83.5	44.0
J111830.28+402554.0	0.1545	2100 ± 110	43.6	0.43 ± 0.02	$2.14^{+0.10}_{-0.11}$	-109.8 ± 40.4	7.70	0.54	-116.1 ± 48.2	43.8
J112328.11+052823.2	0.1013	1660 ± 350	42.2	0.18 ± 0.04	$2.00^{+0.11}_{-0.11}$	11.5 ± 35.4	7.04	0.25	-71.6 ± 7.7	42.8
J114008.71+030711.4	0.0811	1350 ± 80	41.5	0.78 ± 0.07	$1.84^{+0.27}_{-0.28}$	-3.7 ± 22.9	6.52	0.22	-62.0 ± 34.4	42.6
J120442.10+275411.7*	0.1651	5080 ± 420	43.3	0.06 ± 0.02	$1.58^{+0.07}_{-0.08}$	38.4 ± 9.4	8.28	0.12	-232.0 ± 27.7	44.4
J121356.19+140431.3	0.1539	4970 ± 460	42.6	0.15 ± 0.01	$1.48^{+0.18}_{-0.20}$	.....	8.20	0.04	-53.7 ± 113.3	43.4
J121930.87+064334.4	0.0804	1780 ± 70	43.0	0.08 ± 0.01	$2.11^{+0.08}_{-0.08}$	11.5 ± 43.9	7.42	0.54	-61.0 ± 22.5	43.0
J122137.93+043026.1*	0.0947	8530 ± 410	42.0	0.25 ± 0.01	$1.43^{+0.17}_{-0.19}$	21.6 ± 15.9	8.18	0.01	$+2.1 \pm 4.3$	42.9
J123113.66+151127.9	0.1919	3500 ± 190	42.3	0.47 ± 0.03	$2.20^{+0.16}_{-0.15}$	17.9 ± 44.1	7.48	0.12	-83.7 ± 48.5	43.3
J124013.80+473354.8	0.1174	1840 ± 240	41.7	0.75 ± 0.06	$1.48^{+0.45}_{-0.48}$	4.7 ± 51.2	6.72	0.20	-33.1 ± 10.7	43.0
J124210.60+331702.6	0.0437	1470 ± 120	43.0	0.06 ± 0.01	$2.15^{+0.01}_{-0.01}$	-2.9 ± 35.1	7.32	0.60	-173.1 ± 44.5	43.3
J124635.24+022208.7	0.0482	1270 ± 90	41.9	0.45 ± 0.05	$2.36^{+0.10}_{-0.10}$	-118.4 ± 32.8	6.72	0.31	-62.3 ± 43.8	43.0
J130022.15+282402.6	0.0911	3550 ± 140	42.3	0.39 ± 0.01	$1.70^{+0.11}_{-0.12}$	7.5 ± 48.7	7.46	0.12	-7.9 ± 8.2	43.4
J130947.00+081948.2	0.1543	4320 ± 130	43.7	0.10 ± 0.01	$1.46^{+0.04}_{-0.04}$	41.4 ± 24.6	8.43	0.20	-137.1 ± 25.9	44.0
J133141.02-015212.4	0.1454	1570 ± 280	42.1	0.24 ± 0.05	$1.72^{+0.39}_{-0.41}$	-38.7 ± 31.0	7.01	0.22	-27.4 ± 26.8	43.0
J134351.06+000434.7*	0.0737	3300 ± 150	41.7	0.69 ± 0.01	$1.43^{+0.23}_{-0.23}$	18.3 ± 30.8	6.84	0.16	$+0.9 \pm 4.5$	41.6
J134834.94+263109.8*	0.0589	1580 ± 90	42.3	0.11 ± 0.01	$1.79^{+0.23}_{-0.23}$	11.7 ± 37.6	7.11	0.28	-119.5 ± 56.9	42.7
J135435.68+180517.4	0.1509	4190 ± 110	43.9	0.04 ± 0.01	$1.83^{+0.11}_{-0.11}$	.....	8.52	0.25	-142.5 ± 48.9	44.0

Table 1—Continued

SDSS	z	$\mathrm{FWHM}_{\mathrm{H}\beta}$ km s^{-1}	$\log \frac{L_{\mathrm{H}\alpha}}{\mathrm{erg\ s^{-1}}}$	RFe	$\Gamma_{2-10\mathrm{keV}}$	Δv[b] km s^{-1}	$\log \frac{M_{\mathrm{BH}}}{M_\odot}$	L/L_{Edd}	δv km s^{-1}	$\log \frac{L_{\mathrm{X}}}{\mathrm{erg\ s^{-1}}}$
(1)	(2)	(3)	(4)	(5)	(6)	(7)	(8)	(9)	(10)	(11)
J135553.52+383428.7*	0.0502	6500 ± 220	42.4	0.04 ± 0.01	$1.56^{+0.07}_{-0.07}$	22.6 ± 7.3	7.75	0.07	-25.3 ± 7.4	43.2
J135724.51+652505.9	0.1063	1590 ± 190	41.6	0.30 ± 0.05	$1.96^{+0.18}_{-0.23}$	-15.5 ± 27.9	6.40	0.36	-13.2 ± 9.8	42.9
J140251.19+263117.5	0.1875	5900 ± 80	44.1	0.07 ± 0.01	$1.49^{+0.10}_{-0.10}$	104.5 ± 33.2	9.01	0.11	-84.3 ± 26.4	44.2
J140621.89+222346.5	0.0979	4280 ± 110	42.5	1.43 ± 0.04	$1.95^{+0.44}_{-0.42}$	-47.2 ± 44.3	7.83	0.07	-283.1 ± 105.0	42.5
J140700.40+282714.6	0.0766	8240 ± 450	43.5	0.09 ± 0.05	$1.22^{+0.10}_{-0.10}$	61.5 ± 20.6	9.18	0.03	-29.6 ± 15.0	42.5
J141519.50-003021.5	0.1347	2260 ± 190	41.8	1.21 ± 0.11	$2.15^{+0.09}_{-0.09}$	-304.5 ± 58.3	6.94	0.14	-99.6 ± 67.6	42.9
J141700.82+445606.3	0.1136	2590 ± 150	42.8	0.86 ± 0.07	$1.93^{+0.09}_{-0.09}$	.....	7.73	0.18	-276.9 ± 49.7	43.5
J143452.45+483942.7	0.0365	4520 ± 190	43.0	0.004 ± 0.003	$1.58^{+0.21}_{-0.23}$	-39.5 ± 45.4	8.23	0.08	$+14.8 \pm 6.3$	43.1
J145108.76+270926.9	0.0645	3040 ± 100	42.6	0.79 ± 0.03	$2.27^{+0.06}_{-0.06}$	9.9 ± 12.9	7.50	0.20	-103.7 ± 10.6	43.3
J150626.44+030659.9	0.1734	2270 ± 400	42.8	0.15 ± 0.01	$1.79^{+0.02}_{-0.25}$	.....	7.49	0.28	-147.7 ± 20.8	43.6
J151600.96+000949.7	0.1712	4440 ± 190	42.3	0.09 ± 0.11	$1.68^{+0.07}_{-0.07}$	.....	7.81	0.05	-45.2 ± 38.0	43.4
J155909.63+350147.5	0.0311	1700 ± 110	41.7	1.53 ± 0.14	$2.15^{+0.06}_{-0.07}$	-70.9 ± 21.7	6.42	0.41	-18.7 ± 23.2	42.9
J160452.45+240241.6*	0.0876	2710 ± 780	42.7	0.17 ± 0.04	$1.78^{+0.07}_{-0.07}$	42.7 ± 58.4	7.56	0.21	-17.9 ± 6.0	43.1
J221918.53+120753.1	0.0815	1110 ± 80	42.4	0.19 ± 0.01	$2.47^{+0.12}_{-0.13}$	-26.3 ± 32.6	6.80	0.70	-63.7 ± 27.2	43.1

Note. — The object that shows a Seyfert-1.5 like spectrum is marked by a star. The redshifts given in Column (2) are provided by the SDSS pipelines.

[a]The value is given for Hβ rather than Hα because of the bad observed Hα line profile. See Section 4.3.1 in the text for the details.

[b]The values of Δv are not available for a few objects since the bad constraint on their Hβ narrow peaks.

Table 2: Correlations coefficient matrix related with the hard X-ray photon index versus [O III]λ5007 emission line profile correlations

Property	$\Gamma_{2-10\mathrm{keV}}$	δv	Δv
(1)	(2)	(3)	(4)
(1) $\Gamma_{2-10\mathrm{keV}}$	.....	-0.411(0.0054)	-0.483(0.0022)
(2) RFe	0.408(0.0057)	-0.268(0.0694)	-0.508(0.0011)
(3) $\mathrm{FWHM_{H\beta}}$	-0.673($< 10^{-4}$)	0.269(0.0685)	0.416(0.0077)
(4) M_{BH}	-0.497(0.0008)	-0.073(0.6218)	0.509(0.0011)
(5) L/L_{Edd} ..	0.620($< 10^{-4}$)	-0.418(0.0046)	-0.266(0.0886)
(6) $L_{1.4\mathrm{GHz}}$[a] .	-0.240(0.1510)	-0.170(0.3103)	0.281(0.0929)
(7) $L_{1.4\mathrm{GHz}}$[b] .	0.010(0.8882)	-0.107(0.1362)	0.085(0.2371)

[a]The statistics is based on the 20 sources with detected radio flux taken from the FIRST catalog.

[b]The statistics is based on all the 47 sources through survival analysis.

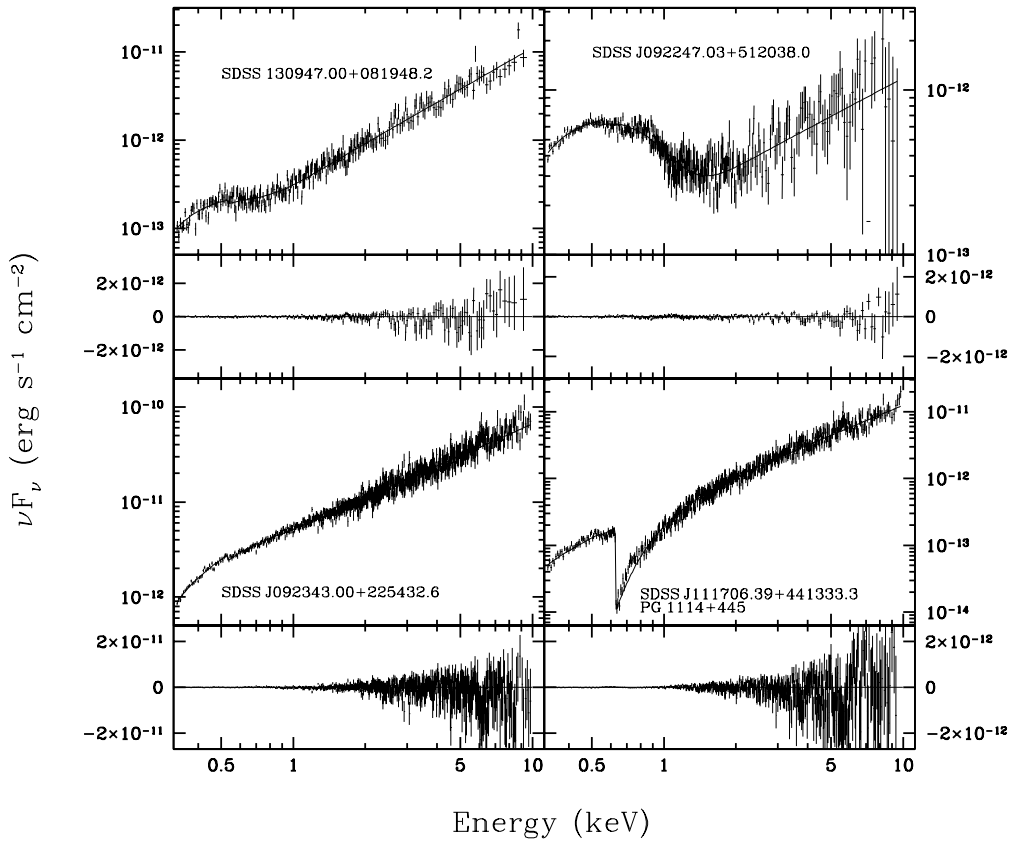

Fig. 1.— Examples of the X-ray spectral modelings. In each panel, the top sub-panel shows the EPIC PN X-ray spectrum in terms of νF_ν and the best-fit spectral model (see Section 3.1 for the details of the used model). A strong absorption edge at 0.72 ± 0.01 keV (rest frame) is required in SDSS J111706.39+441333.3 (PG 1114+445, right-bottom panel) to properly reproduce its observed spectra. The bottom sub-panel shows the deviation of the observed data from the best-fit model in terms of νF_ν.

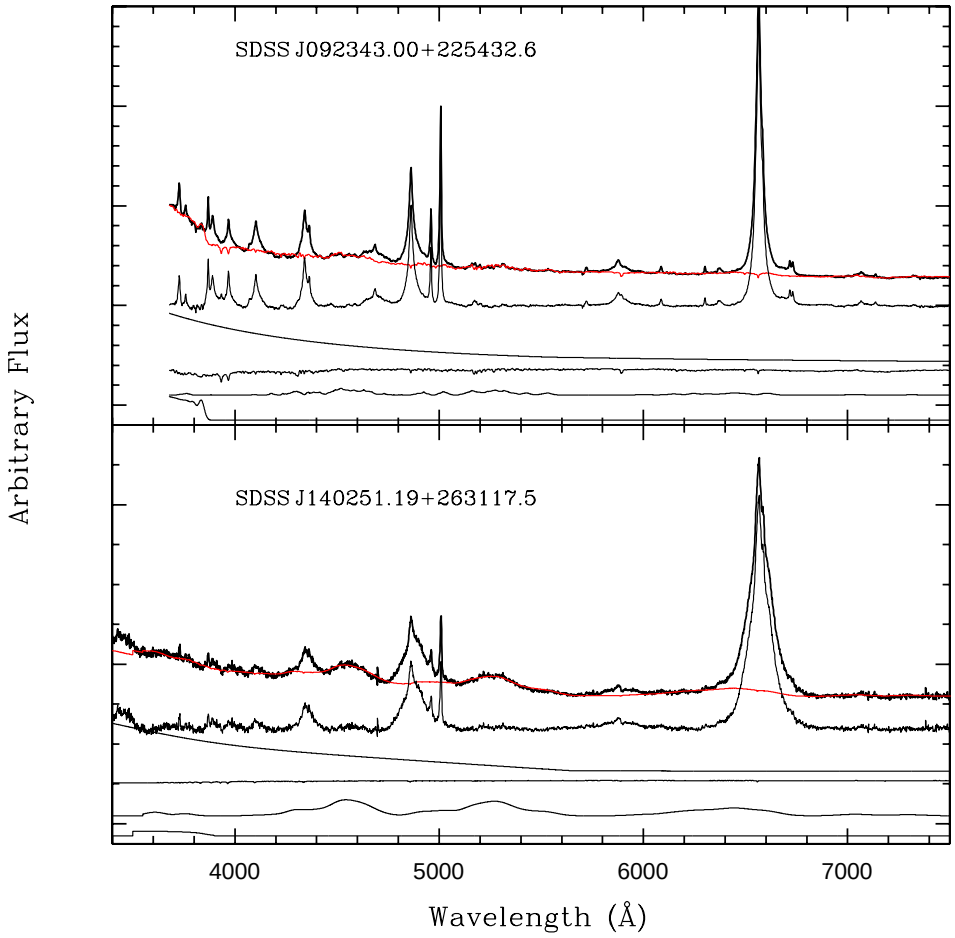

Fig. 2.— Illustration of the modeling and removal of the continuum for two typical sources. In each panel, the top curve shows the observed rest-frame spectrum overplotted by the modeled continuum by the red curve. The continuum-removed emission-line spectrum is shown below the observed one. The modeled continuum is obtained by a reddened linear combination of a broken power law from the central AGN, a starlight component from the host galaxy, the emission from the Fe II complex, the Balmer continuum, and the high order Balmer emission lines, which are plotted in ordinals below the emission-line spectrum. The intrinsic extinction is considered in the modeling by using a Galactic extinction curve with $R_V = 3.1$. All the spectra are shifted vertically by an arbitrary amount for visibility.

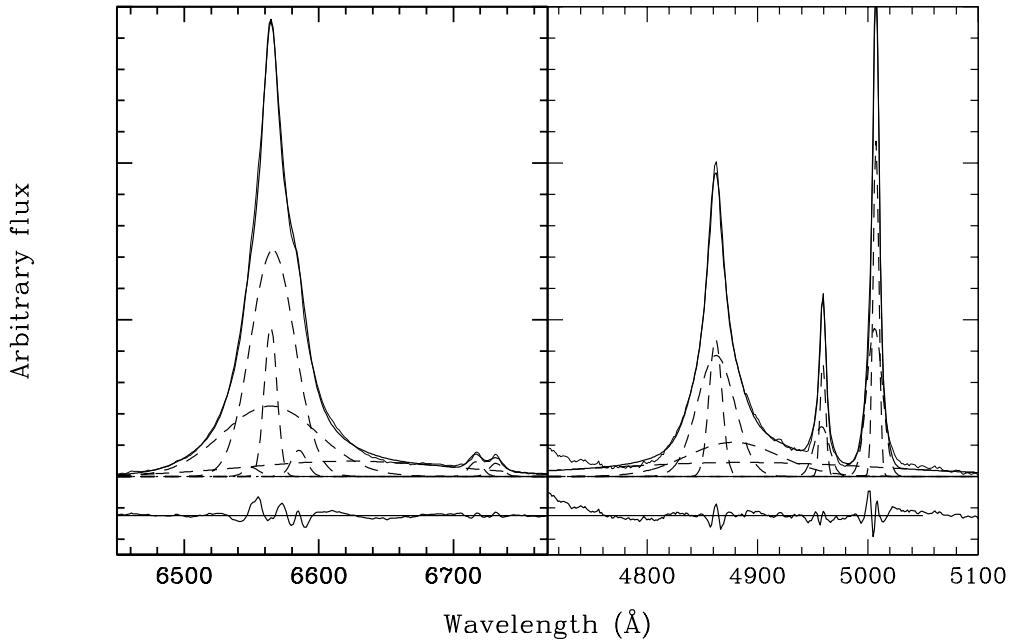

Fig. 3.— Line profile modelings of SDSS J092343.00+225432.6 by a linear combination a set of Gaussian functions for the Hα (left panel) and Hβ (right panel) regions. In each panel, the observed and modeled line profiles are plotted by light and heavy solid lines, in which the modeled continuum has already been removed from the original observed spectrum. Each Gaussian function is shown by a dashed line. The sub-panel underneath each line spectrum presents the residuals between the observed and modeled profiles.

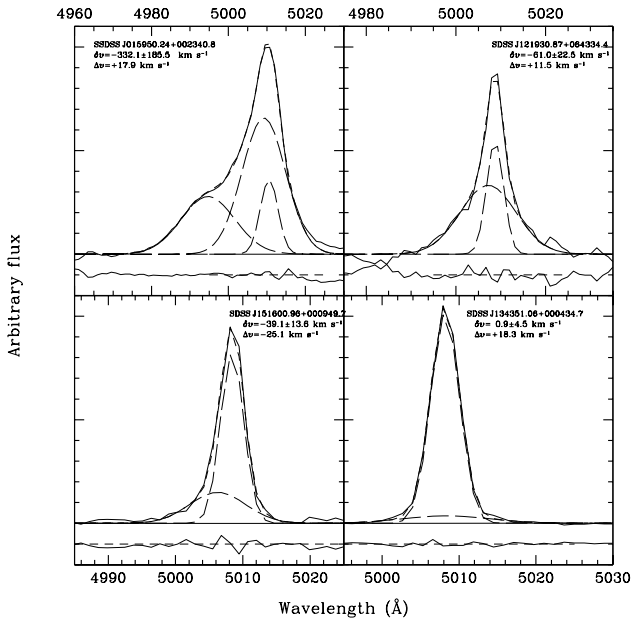

Fig. 4.— [O III]λ5007 line profile modeling by a sum of n Gaussian functions for four typical cases. In each panel, the observed and modeled line profiles are plotted by solid and dashed lines, respectively. The sub-panel underneath each line spectrum presents the residuals between the observed and modeled profiles. All the spectra are transformed to rest frame based on the redshifts given by the SDSS pipelines.

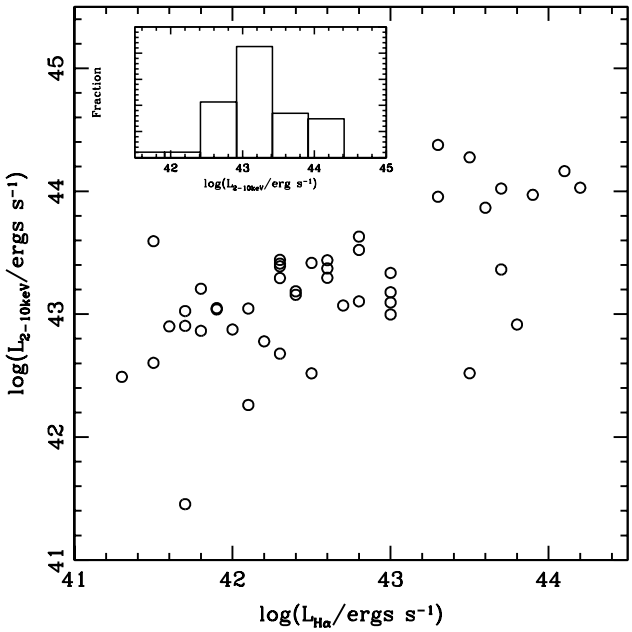

Fig. 5.— Hard X-ray Luminosity in the energy bandpass 2-10 keV ($L_{2-10\mathrm{keV}}$) plotted against the luminosity of broad Hα emission. The inset panel shows the distribution of $L_{2-10\mathrm{keV}}$.

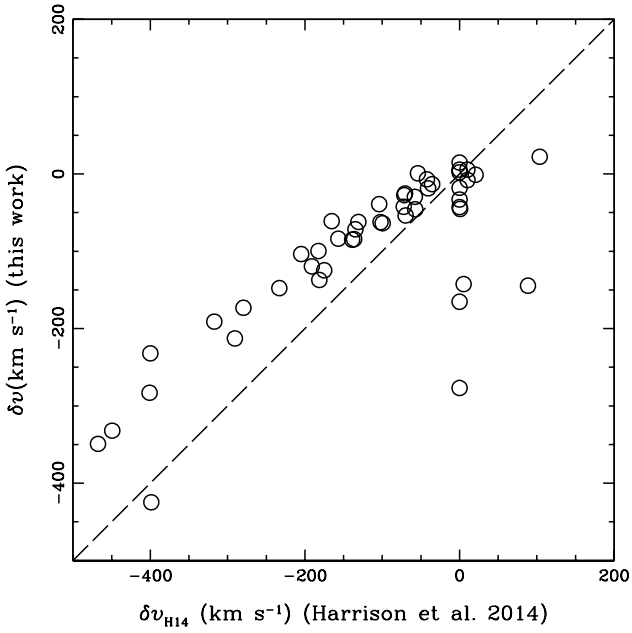

Fig. 6.— A comparison between the value of δv used in this paper and the velocity offset δv_{H14} defined in Harrison et al. (2014). See the text for the details of the definition of δv_{H14}. A ratio of 1 is presented by the dashed line.

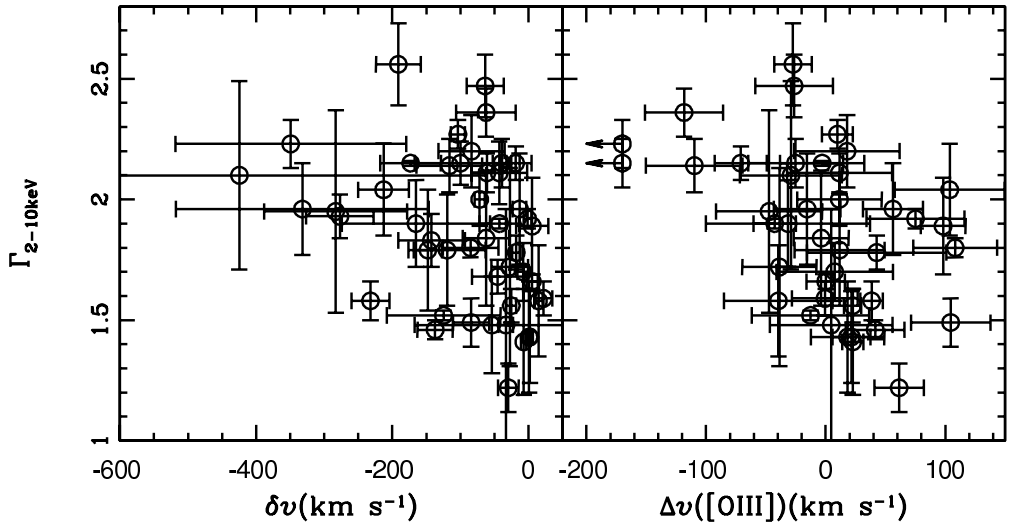

Fig. 7.— *Left panel:* The hard X-ray photon spectral index ($\Gamma_{2-10\mathrm{keV}}$) plotted as a function of [O III]λ5007 line profile asymmetry parameter δv. *Right panel:* The same as the left one but for [O III] line bulk velocity shift with respect to the Hβ narrow peak (Δv). The two points associated with left arrows mark the objects with Δv as large as ~ 300 km s^{-1}.

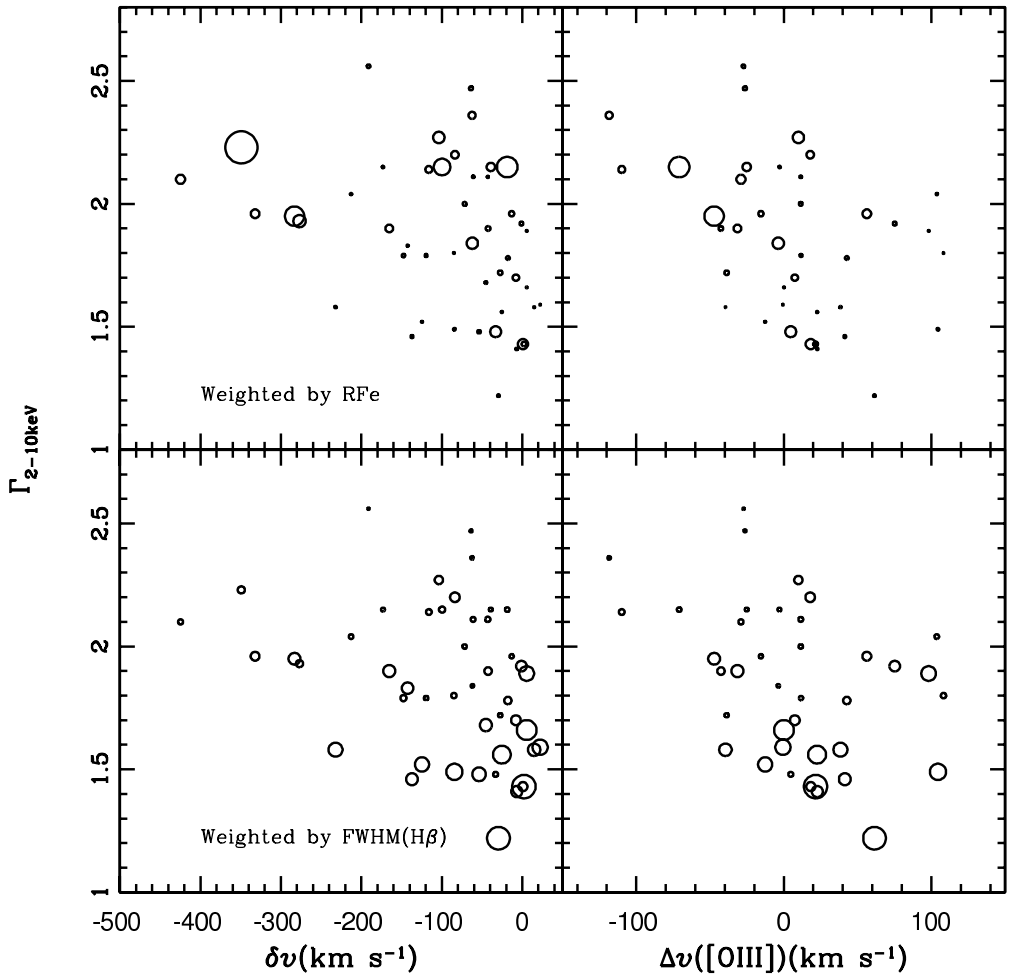

Fig. 8.— *Bottom panels:* The $\Gamma_{2-10\mathrm{keV}} - h_3$ (left) and $\Gamma_{2-10\mathrm{keV}} - \Delta v$ (right) correlations in which the size of each point is proportional to the measured FWHM of Hβ broad emission line. *Top panels:* The same as the bottom ones but for the point size that is proportional to RFe.

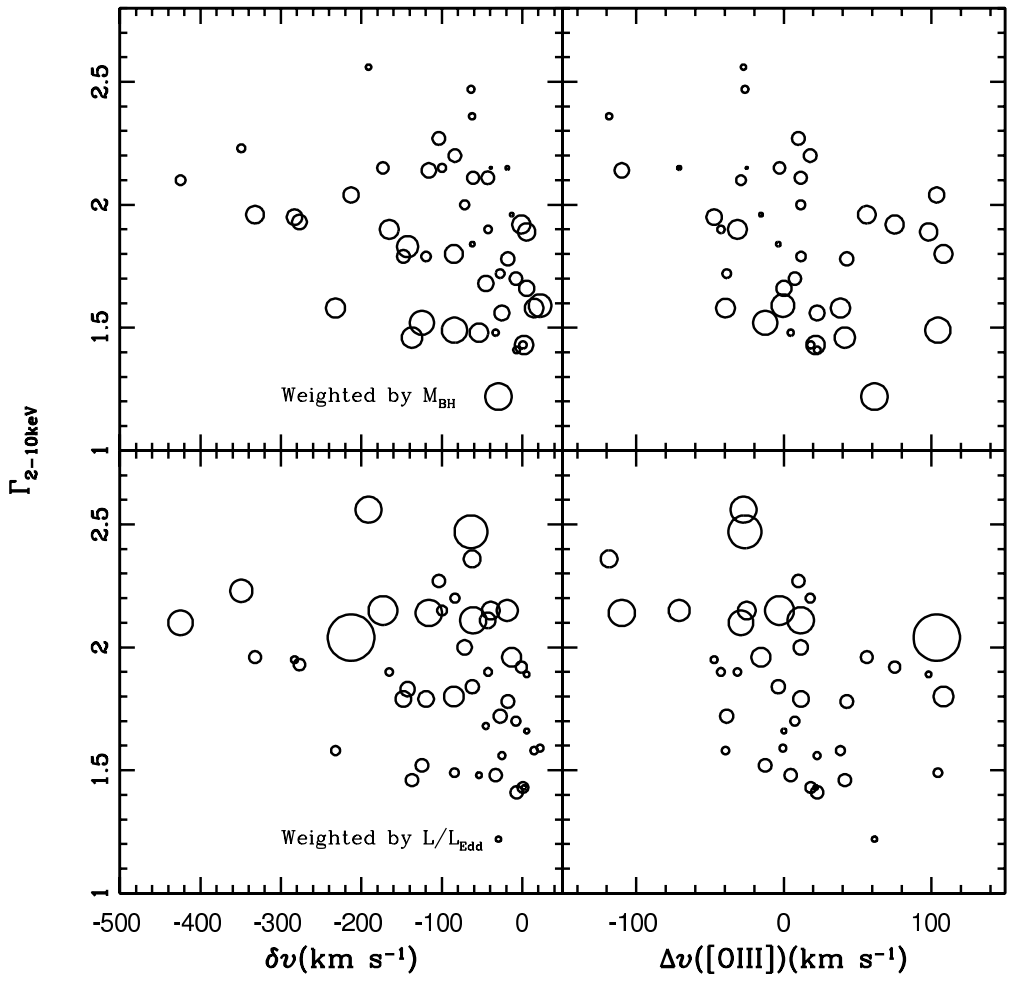

Fig. 9.— *Bottom panels:* The $\Gamma_{2-10\mathrm{keV}} - h_3$ (left) and $\Gamma_{2-10\mathrm{keV}} - \Delta v$ (right) correlations in which the size of each point is proportional to the estimated L/L_{Edd}. *Top panels:* The same as the bottom ones but for the point size that is proportional to M_{BH}.

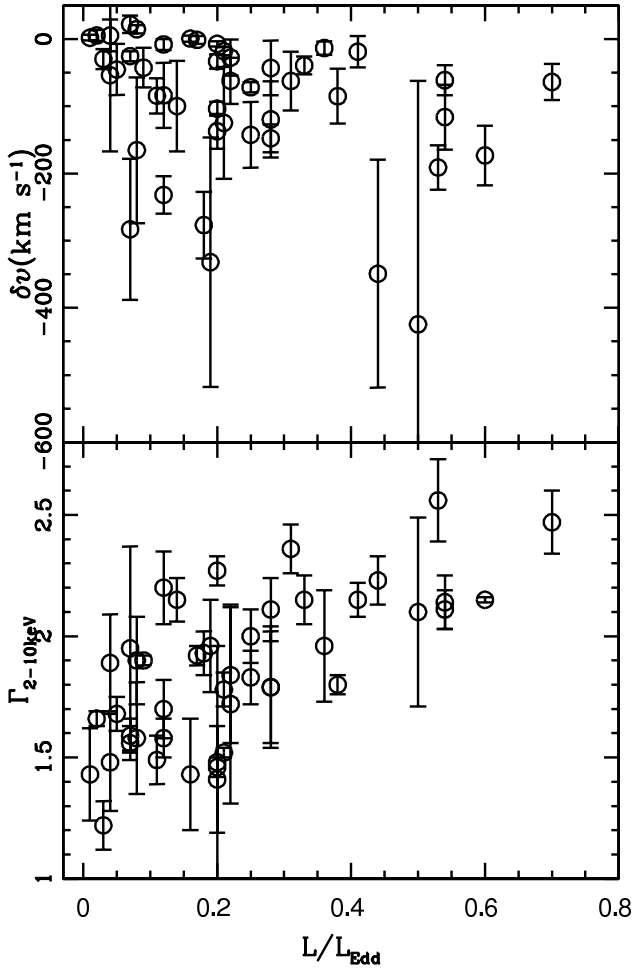

Fig. 10.— $\Gamma_{2-10\mathrm{keV}}$ (*bottom panel*) and δv (*top panel*) are plotted as a function of L/L_{Edd}.

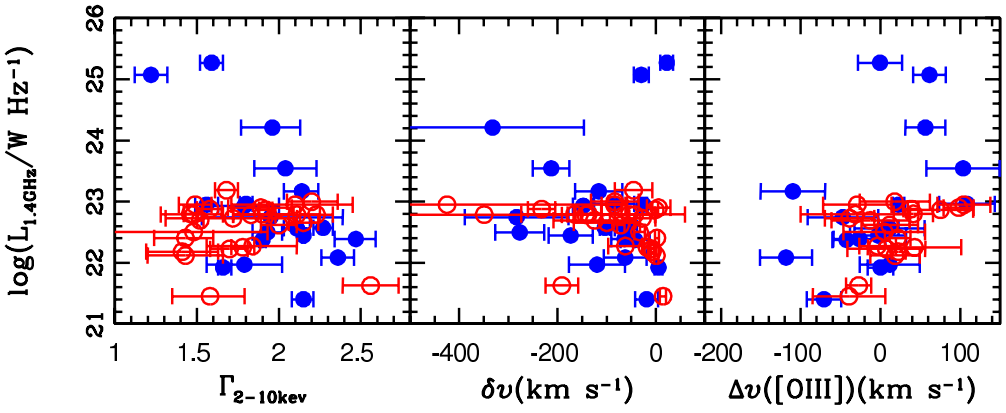

Fig. 11.— Calculated radio luminosity at 1.4GHz (rest frame) plotted against $\Gamma_{2-10\mathrm{keV}}$, δv and Δv in the left, middle and right panels, respectively. The sources with a detected radio flux is shown by the blue solid points, and the ones with a flux upper limit by the red open points.